Improving the slow extraction efficiency of the CERN Super Proton Synchrotron

Brunner Kristóf

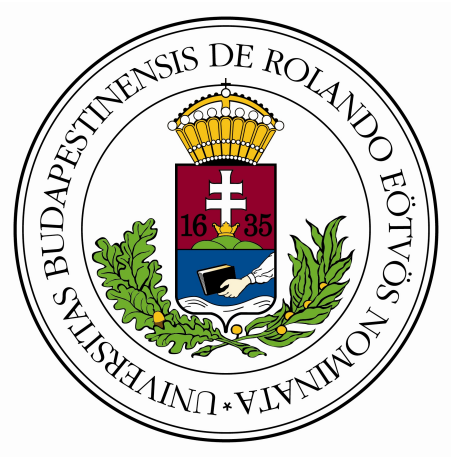

Faculty of Science
Eötvös Loránd University

Supervisors: Barna Dániel, Wigner RCP
Christoph Wiesner, CERN

May 2018

Contents

1

Introduction

In the last few decades, the use of particle accelerators became widespread not only in different fields of physics (eg. particle physics, particle astrophysics) but also in other sciences [1]. Two interesting examples of this are biology and medicine. Scientists used synchrotron light produced by electron machines to solve the 3D structure of different proteins. A few particle accelerators were built in the last years with the main purpose of offering people a new form of radiation therapy, called the ion beam therapy (e.g. MedAustron [2]). Proton and heavy ion beams have a much better-localised energy deposition region, which makes them the perfect candidate for treatments that need deep penetration of the beam.

On the other end of the spectrum, in art history particle beams can be used to analyse works of art in a non-destructive way [3]. In material science, particle accelerators play a role as a source of photon, neutron and ion beams. For example at ISIS scientists used neutron reflectivity and small-angle neutron scattering to analyse how the drug amphotericin works [4].

Due to many fields using particle accelerators for many different reasons, their requirements for the beam can vary greatly from each other, and there is always room for improvement. Accelerator physics is sometimes seen as the "servant" of particle physics or heavy ion physics, but in reality while particle physics is important and a large portion of accelerator development is happening in nuclear research centres (e.g. CERN), accelerator physics did spring forth in the last decade, and became an essential part of modern-day technology and medicine.

It is believed that in the upcoming decade particle accelerators will spread even further, and become more and more common in an ordinary university laboratory for example.

One of the most critical parts of particle acceleration is the extraction of the particles. The quality of the beam strongly depends on the method used for extraction. There are many studies aimed to achieve better, quicker, more loss efficient extraction of particle accelerators. This work was done to study a possibility to increase the efficiency of the so-called slow extraction.

2

CERN accelerator complex

The European Organization for Nuclear Research (CERN) is one of the greatest science institutes of the world. It was established in 1954 on the Franco-Swiss border in the suburb of Geneva. It has 22 member states and several associate member states, and “observers”.

2.1 Accelerators

CERN provides primary or secondary particle beams with energies up to 7 TeV to several different particle physics experiments, which require different intensities, energies, and luminosities from the beam source. The accelerator complex of CERN is able to meet the different requirements due to having a wide range of accelerators with different parameters [5]. Most of the individual accelerators can extract particles at least in 2 ways, either injecting the beam into the next accelerator or extracting it towards a fixed target experiment. The whole map of the CERN accelerators can be seen in Fig. 2.1.

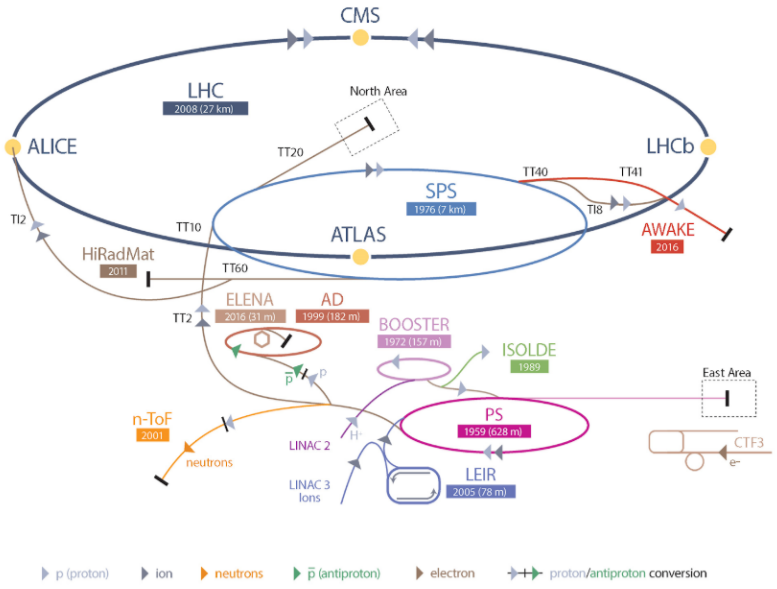

Figure 2.1: Map of CERN accelerator complex

Protons are provided to the accelerator complex by a duoplasmatron source, which strips off the electrons of the H2 molecules and separates the molecules to single protons. They enter the LINAC 2 linear accelerator which accelerates them to 50 MeV. With this energy, they proceed to the Proton Synchrotron Booster (PSB in short) which consists of 4 superimposed synchrotron rings. They accelerate the protons to 1.4 GeV, and inject the particles to the Proton Synchrotron (PS), and also to ISOLDE, which is a heavy ion experiment. The maximum energy of the PS is 25 GeV. It provides beam to the East Area, some neutron experiments, the antiproton experiments in the Antiproton Factory, and injects to the Super Proton Synchrotron (SPS).

In the Antiproton Factory, the proton beam is shot into a metal target. The collision creates a lot of particles (photons, electrons, positrons, pions, kaons, protons, and antiprotons). For further use, the antiprotons are collected, cooled, and decelerated to 5.3 MeV in the Antiproton Decelerator (AD). The Extra Low Energy Antiproton Ring (ELENA) is still in the experimental phase but will be decreasing the energy of the antiprotons to around 100 keV. There is a wide range of experiments at the AD, most of which are low-energy, high-precision experiments, measuring the properties of antiprotons and antihydrogen.

The SPS is around 10 times bigger than the PS and is able to accelerate protons to 450 GeV. It is the injector of the Large Hadron Collider (LHC) while also provides beam to the North Area (NA) and in the near future to the Proton Driven Plasma Wakefield Acceleration Experiment (AWAKE).

The LHC is the highest energy particle accelerator made by man so far. The maximum achieved energy (per beam) is 7 TeV, which means a total of 14 TeV centre-of-mass energy can be analyzed by the 4 experiments (ATLAS, CMS, LHCb, ALICE) located around the ring. The LHC is filled in 40 minutes from the SPS, and after the ramping of the magnet strength and particle energy in parallel, it operates up to 7-8 hours in collision mode before the beam is extracted to the beam dump.

Some nominal values of the LHC beam are:

- ~2800 particle bunches
- Each bunch contains 1.15E+11 protons
- Each bunch is ~30 cm long and its transverse diameter is in the order of a mm
- At injection, the particles move at 0.999997828 times the speed of light, which goes up to 0.999999991 times c at maximum energy
- The total beam energy is 362 MJ

2.2 Experiments

There are several experiments running at CERN all the time, our goal here is just to show a short overview of them, not to provide a comprehensive list.

The two main families of experiments at CERN are the collider- and the fixed target (FT) experiments.

2.2.1 Colliders

As known from its name the LHC is a collider ring, meaning that it has two beams running in opposite directions (in separate beampipes), and there are 4 crossing points at the centres of the 4 experiments. One of the biggest difficulty of a collider is that the beam has to be squeezed to a tiny cross-section ($\sim 16\ \mu\mathrm{m}$), to increase the chance of two protons (or lead ions) colliding. However, the great advantage of a collider is that the achievable centre-of-mass energy can be much higher.

The main goal of the ATLAS and the CMS experiments (and the main goal of the full LHC project) was to find the Higgs-boson, the last missing particle of the standard model. The discovery of the Higgs-boson was announced on the 4th of July, 2012, with a mass between 125 and 127 GeV This was probably the greatest discovery in particle physics in the 21st century.

The LHCb is studying CP violation and has announced in 2013 that CP violation has been discovered in strange B meson decays. ALICE is mostly studying heavy ion (e.g. lead ion) collisions, for example, collecting data on the behaviour of the quark-gluon plasma (QGP) which is a state of particles at ultra-high temperatures ($\sim 10^{12}\ K$) and high density.

2.2.2 Fixed target experiments

Most of the experiments at CERN are shooting beam into a fixed target and put detectors around or behind this target, to observe the collisions products. The advantage of the fixed target experiments is that the target's material and thickness can be changed easily, and high luminosities can be achieved without squeezing the beam down to $\sim 20\ \mu m$.

An example fixed target experiment is the NA61/SHINE experiment located in the Northern area. It receives its beam from the SPS through slow extraction (discussed later). When hadron-nucleus collisions are studied, the beam (with an energy around 400 GeV) hits a beryllium plate target, which produces a secondary beam of particles. Then a given particle type can be selected from the secondary beam and sent towards the experiment. There are also nucleus-nucleus collisions studied in order to analyze the transition line between QGP and hadron gas [6].

2.3 Current and future demands of fixed target experiments

Most high-energy fixed target experiments require a "semi-continuous" beam. Part of the reason for this is that if the content of the SPS would be extracted in one turn and shot into a target, the energy deposition would get really high, destroying the target. The other reason is that the data acquisition system of the experiments could go to saturation, and the reconstruction software would have difficulties disentangling pile-up events, and identifying individual particle trajectories. As a comparison, in a collider experiment the usual pileup (number of interactions in one bunch crossing) is 10-20 which is only $1.74 \cdot 10^{-8}\%$ of all the particles in one bunch.

Therefore the experiments typically require spills of reduced particle density for longer time. The way to achieve this is to have a so-called multi-turn slow extraction where in every turn a tiny portion of the beam is cut off and extracted towards the experiments, while the rest still keeps circulating in the ring. This process is the source of around 5% loss increase since a "blade" has to

be inserted into the blown-up beam to cut off the extracted part. This process will be explained later in details. Particles scattered on this "blade" can hit the beampipe downstream of the extraction point. Activation of the surrounding material is a serious risk factor for the maintenance personnel and limits the time they can spend in the tunnel. This gives a limit on the allowed extraction rate during standard operation, which is below the acceptable proton intensity by the current, or especially the planned fixed target experiments.

Currently the slow extraction lasts for $\sim 2 \cdot 10^5$ turns, or ~ 4 s. During this time $\sim 4 \cdot 10^{13}$ protons are extracted semi-continuously. However, the experiments request higher number of protons-on-target (POT), which can only be achieved by reducing the losses of the slow extraction first. This is the motivation behind our study.

3

Introduction to accelerator physics

3.1 History of linear and circular accelerators

Particle accelerators have been used widely in the last century to analyze the behaviour of particles at high energy and to understand the smallest "building blocks" of our universe. The first electrostatic accelerators (e.g. Van de Graaff generator) introduced the idea of using a high voltage electrostatic field to give energy to charged particles. The limitation of this concept is that the field gets harder to produce and maintain the higher its voltage is [7].

The idea of radio frequency (RF) linear accelerators is based on the fact that the particles do not have to be accelerated in one step. If the acceleration process is divided into several steps, then the energy gain in one step can be lower, and this way the acceleration field easier to maintain. The concept is visible in Fig. 3.1.

Using this concept of RF LINAC the maximum achievable energy increased significantly, but since each particle passes every acceleration gap only once, the energy is still proportional to the size of the machine.

The first circular accelerator, the cyclotron, was invented by Ernest Orlando Lawrence in 1932. Its concept is based on the fact that for non-relativistic particles the radius (and the circumference) of the path of a charged particle inside a homogeneous magnetic field is proportional to its velocity [8], because

$$F_L = q \cdot \mathbf{v} \times \mathbf{B},$$
$$F_L = m \cdot \frac{v^2}{r},$$

where F_L is the Lorentz force, q is the charge, $\mathbf{v}$ is the velocity, m is the mass of the particle, while $\mathbf{B}$ is the magnetic field strength, and r is the radius of the particle trajectory. From these two equations comes that

$$r = \frac{mv}{q\,|\mathbf{B}|},$$
$$r\,|\mathbf{B}| = \frac{p}{q},$$

where p is the momentum of the particle, and p/q is called magnetic (or beam) rigidity. The revolution frequency (called "cyclotron frequency") of the particle is independent of its energy.

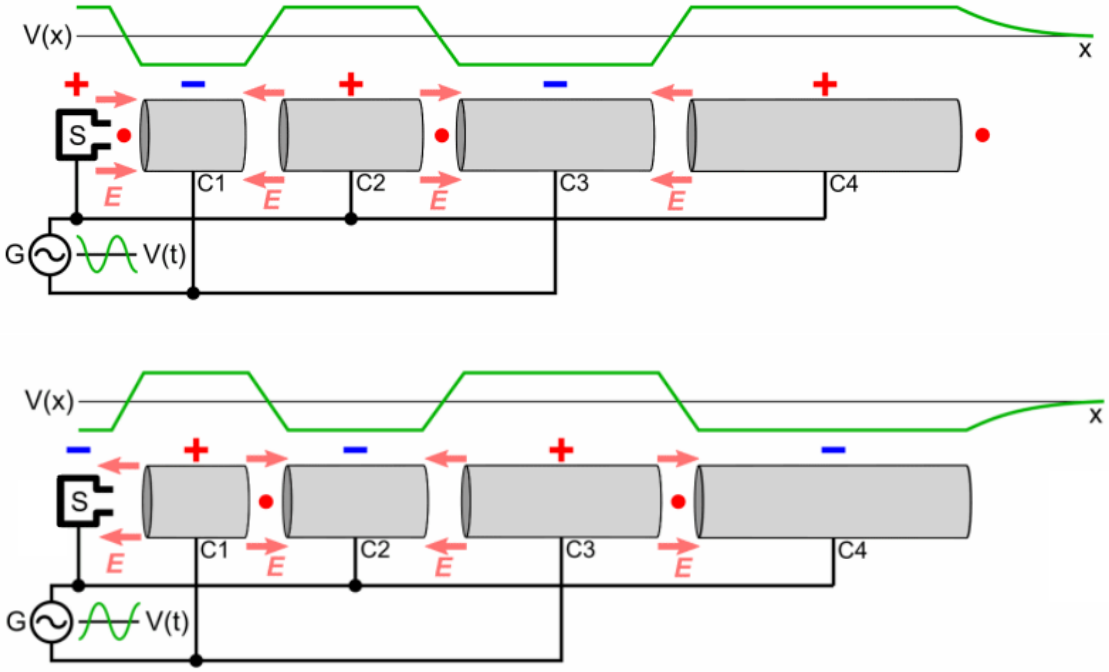

Figure 3.1: Concept of radio frequency linear accelerators

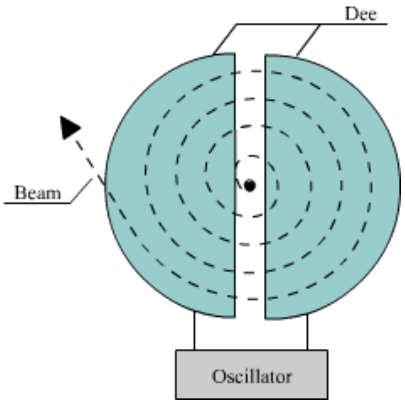

Figure 3.2: Concept of a simple cyclotron

This means that an RF electrostatic field (without any modulation) is able to accelerate particles inside homogeneous magnetic field as seen in Fig 3.2.

As the velocity of the particles approaches the speed of light, this so-called cyclotron resonance condition breaks down, because the circumference of the particles increases with p and not v.

The concept of the cyclotron opened a whole new area of study called circular accelerators, the basics of which is that if the particles can pass the same accelerator cavity (or any voltage gap, etc) multiple times, then the maximum achievable energy will not be proportional to the size of the machine, but rather the number of acceleration steps or turns.

The difficulty comes from the fact that the beam has to stay stable for several turns. There are several possibilities to focus and stabilize the beam, while also bring it to the acceleration point

again (e.g Betatron, FFAG) of which we will concentrate on the synchrotrons only (all the discussed circular machines at CERN are synchrotrons).

To understand some main phenomena of accelerators we need to understand how the focusing works in a synchrotron, or in other terms, transverse beam dynamics.

3.2 Design orbit, focusing

The trajectory of a particle travelling around in an accelerator with the nominal momentum, and perfectly aligned is called the ideal or design orbit. In a synchrotron, this is a closed orbit meaning that after a full turn the particle returns to the exact same position with exactly the same momentum as before. Some kind of focusing has to be used to keep a non-ideal particle close to the design orbit. In synchrotrons, this is done by quadrupole magnets.

The magnetic field of a quadrupole magnet is visible in Fig. 3.3. It is easy to see that a (positively/negatively) charged particle travelling in the (positive/negative) z-direction is focused in the x-direction (forces acting on it point inwards) while defocused in the y (forces point outwards).

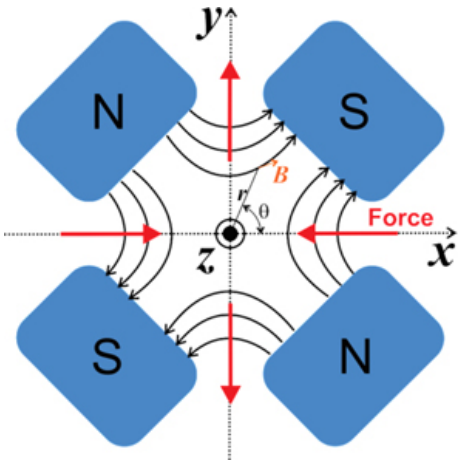

Figure 3.3: Magnetic fields, and the focusing or defocusing forces in a quadrupole magnet

If another quadrupole is used after the first one rotated by $90°$, then it will focus in the y-direction while defocusing in the x. The alternating arrangement of focusing and defocusing elements gives a net focusing effect, which is called alternating gradient focusing (AGF) or strong focusing. This lattice (FODO lattice) can keep the beam close to the design orbit. Non-ideal particles are oscillating around the design orbit.

Higher order multipoles (usually sextupoles) are also used in synchrotrons but we will return to the reason for this at the end of the chapter.

3.3 Betatron oscillation, the behaviour of single particles

We will use the coordinates x, y, s for parametrization of the ring where s is the longitudinal coordinate and it goes from 0 to 1, x and y are the transverse coordinates. The other three usual parameters used are p_0 as the longitudinal momentum, $x' = \mathrm{d}x/\mathrm{d}s = p_x/p_0$ and $y' =$

$\mathrm{d}y/\mathrm{d}s = p_y/p_0$ as the angle of a particle trajectory with respect to the design orbit [9]. In this short introduction, only the x transverse direction is taken into account. Coupling between the horizontal and vertical plane is neglected.

To understand the beam dynamics a bit more, we introduce the quadrupole focusing strength as a function of s:

$$K(s) = \frac{q}{p_0}\frac{\mathrm{d}B_y}{\mathrm{d}x}$$

where q is the charge of the particle, p_0 is the longitudinal momentum, and B_y is the y component of the magnetic field. Inside dipoles B_y is constant so $K(s)$ is zero. As described in [10], the equation of motion, also called Hill's equation, for on-momentum (momentum is equal to the design momentum) particles is:

$$f''(s) + \left(\frac{1}{\rho^2(s)} + K(s)\right)x(s) = 0,$$

or

$$x''(s) + \widetilde{K}(s)x(s) = 0,$$

where $\rho(s)$ is the bending radius of the design orbit (zero inside quadrupoles, nonzero inside dipoles due to geometrical focusing), and $K(s)$, $\rho(s)$ and $\widetilde{K}(s)$ is periodic in s. This is a so-called pseudo-harmonic oscillator equation (if $\widetilde{K}(s)$ would be constant it would be a harmonic oscillator), and it can be shown that the general solution is:

$$x(s) = \sqrt{\epsilon}\sqrt{\beta(s)}\cos(\Phi(s) + \Phi_0)$$

where ϵ, and Φ_0 are integration constants, $\beta(s)$ is called the beta function, and $\Phi(s)$ is the "phase advance" of the particle in its own pseudo-harmonic oscillation, for which the following equations holds:

$$\beta = \frac{1}{\mathrm{d}\Phi/\mathrm{d}s}.$$

The beta function is a unique and periodic function of the longitudinal position s, and it is completely determined by the accelerator lattice (i.e. the sequence of beamline elements such as quadrupoles, dipoles and drift spaces). The tune of a given optics is the number of oscillations per full turn:

$$Q = \frac{1}{2\pi}\oint\frac{ds}{\beta(s)}$$

We define the alpha and gamma functions as:

$$\alpha(s) = -\frac{1}{2}\beta'(s)$$

$$\gamma(s) = \frac{1+\alpha(s)^2}{\beta(s)}$$

3.4 The Twiss-ellipse, the behaviour of the beam

It is shown in [11] that the following equation holds at any point around the circumference of the ring:

$$\epsilon = \gamma(s)x(s)^2 + 2\alpha(s)x(s)x'(s) + \beta(s)x'(s)^2$$

This is the equation of an ellipse (Twiss-ellipse), which is illustrated in Fig. 3.4. The parameters α, β and ϵ are the Twiss-parameters or Courant-Snyder parameters. Since ϵ is a constant of motion, at a given position s a particle will always find itself on the same ellipse corresponding to that location around the ring, after any number of complete turns. The Twiss-ellipse changes shape around the ring circumference, described by the $\alpha(s)$ and $\beta(s)$ functions.

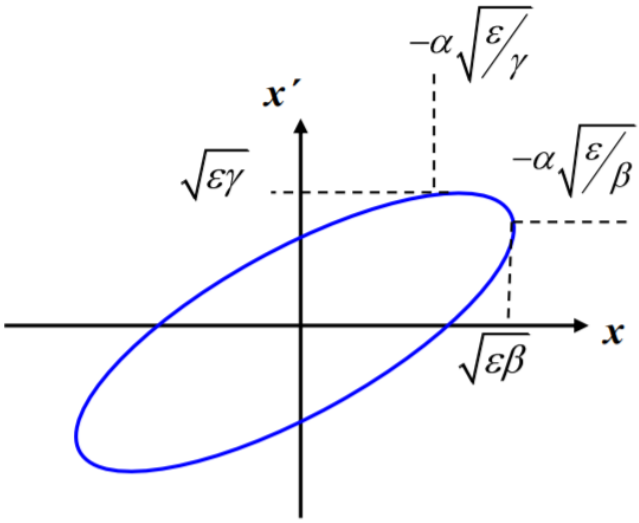

Figure 3.4: The Twiss-ellipse [11].

Usually, in accelerator physics, it is better to analyze the beam as a whole, and not as the collection of single particles. This way the simulation of the beam gets much more resource efficient. The distribution of the beam particles in one transverse phase space (x, x') can typically be approximated by a 2-dimensional Gaussian distribution, which has elliptical equipotentials. If at some location around the ring this ellipse is coincident with the Twiss-ellipse of the accelerator, the beam distribution will follow the evolution of the Twiss-ellipse throughout the ring.

According to Liouville's theorem, in a conservative system, the phase space area occupied by an ensemble of particles is constant. This is in accordance with ϵ (which is the area of the Twiss ellipse divided by π) being a constant of motion. The ϵ parameter of the equipotential ellipse of the Gaussian beam distribution, which contains a given fraction of the particles, is called the beam emittance. The ellipse corresponding to the 3σ emittance of the beam contains, for example, 99.7% of the particles.

To understand the evolution of the Twiss ellipses, one should analyze the "movement" of particles outside of quadrupoles first. Each particle moves in the x or $-x$ direction, and the "speed" of their movement is proportional to the x' coordinate of the particle as shown in Fig. 3.5.

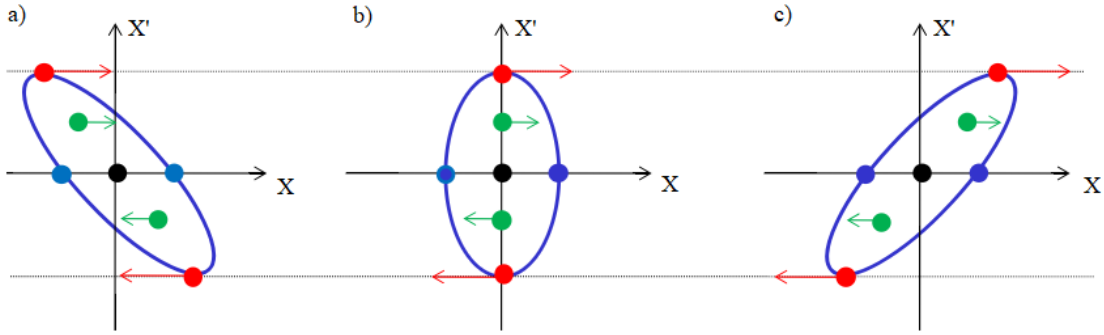

Figure 3.5: Change of the Twiss ellipse in drift space or dipole magnet. Converging beam (a), beam waist (b) and diverging beam (c).

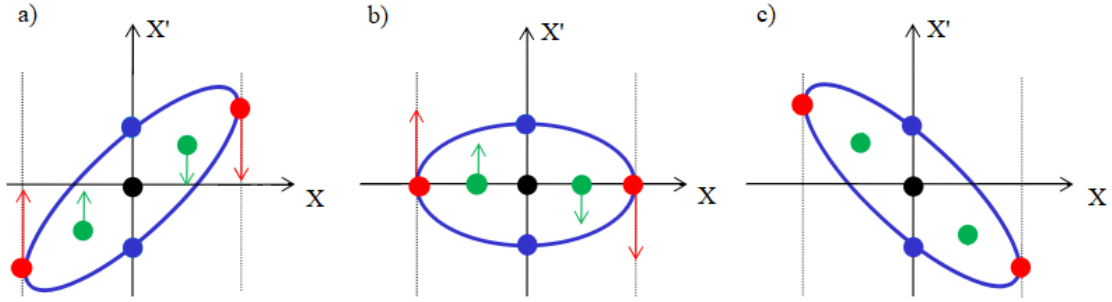

Figure 3.6: Focusing the beam with a quadrupole. Divergent beam enters focusing quadrupole (a), quadrupole kick is applied (b), convergent beam leaves the quadrupole (c).

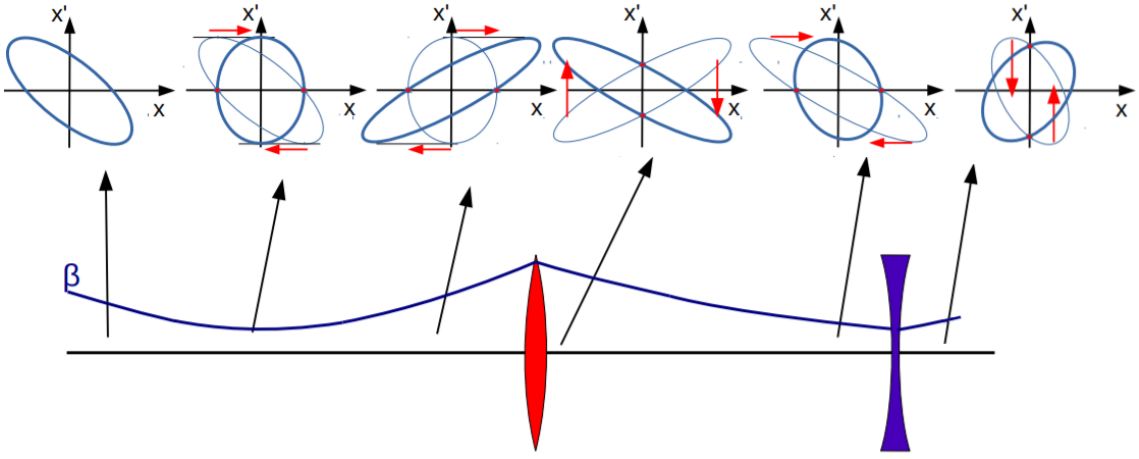

Figure 3.7: Twiss ellipse "evolving" in a FODO lattice. Image taken from [12].

The quadrupole can be approximated as a thin lens because the focal length is much longer than the length of the magnet (analogy with optics). The angle of the particle, in this case, is kicked without changing the position ($\Delta x' = 1/f \cdot x$, where f is the quadrupole focal length). This way a divergent beam can be made convergent with a focusing quadrupole kick, as seen in Fig. 3.6. The periodic change of the Twiss ellipse inside a complete FODO lattice can be seen in Fig. 3.7.

3.5 Normalised phase space

It is usually beneficial to use the so-called normalized conjugate phase space coordinates for simulations. These can be calculated from the real phase space coordinates using the following s dependent matrix:

$$\begin{pmatrix} x_{norm}(s) \\ x'_{norm}(s) \end{pmatrix} = \begin{bmatrix} \frac{1}{\sqrt{\beta(s)}} & 0 \\ \frac{\alpha(s)}{\sqrt{\beta(s)}} & \sqrt{\beta(s)} \end{bmatrix} \begin{pmatrix} x(s) \\ x'(s) \end{pmatrix},$$

While the inverse transformation is:

$$\begin{pmatrix} x(s) \\ x'(s) \end{pmatrix} = \begin{bmatrix} \sqrt{\beta(s)} & 0 \\ -\frac{\alpha(s)}{\sqrt{\beta(s)}} & \frac{1}{\sqrt{\beta(s)}} \end{bmatrix} \begin{pmatrix} x_{norm}(s) \\ x'_{norm}(s) \end{pmatrix}.$$

The reason for this coordinate transformation is that in the normalized phase space the particle trajectory is a circle inside dipoles, quadrupoles, and empty drift space. This helps a lot to illustrate and intuitively understand transverse phenomena in accelerator rings.

The process of particle tracking in the ring using the normalized phase space is the following:

- The alpha and beta function has to be calculated from the optics of the ring only once
- It is also beneficial to calculate the phase advance between each two object using the formula:

$$\Phi(s_1, s_2) = \int_{s_1}^{s_2} \frac{1}{\beta(t)} \mathrm{d}t$$

- When tracking a particle travelling from s_1 to s_2 first the normalized phase space coordinates have to be calculated from the real ones:

$$\begin{pmatrix} x_{norm}(s_1) \\ x'_{norm}(s_1) \end{pmatrix} = \begin{bmatrix} \frac{1}{\sqrt{\beta(s_1)}} & 0 \\ \frac{\alpha(s_1)}{\sqrt{\beta(s_1)}} & \sqrt{\beta(s_1)} \end{bmatrix} \begin{pmatrix} x(s_1) \\ x'(s_1) \end{pmatrix},$$

- The particle is rotated in the normalized phase space with the corresponding $\Phi(s_1, s_2)$ phase advance:

$$\begin{pmatrix} x_{norm}(s_2) \\ x'_{norm}(s_2) \end{pmatrix} = \begin{bmatrix} \cos\left(\Phi(s_1, s_2)\right) & \sin\left(\Phi(s_1, s_2)\right) \\ -\sin\left(\Phi(s_1, s_2)\right) & \cos\left(\Phi(s_1, s_2)\right) \end{bmatrix} \begin{pmatrix} x_{norm}(s_1) \\ x'_{norm}(s_1) \end{pmatrix},$$

- Finally the real phase space coordinates at s_2 can be acquired using:

$$\begin{pmatrix} x(s_2) \\ x'(s_2) \end{pmatrix} = \begin{bmatrix} \sqrt{\beta(s_2)} & 0 \\ -\frac{\alpha(s_2)}{\sqrt{\beta(s_2)}} & \frac{1}{\sqrt{\beta(s_2)}} \end{bmatrix} \begin{pmatrix} x_{norm}(s_2) \\ x'_{norm}(s_2) \end{pmatrix}.$$

Of course, each nonlinear element, or special object (e.g. higher order multipole magnet, collimator) needs separate calculation, but the transfer of the particles between these elements is one single matrix multiplication.

3.6 Tune and resonances

As described before the tune of a ring can be calculated as the phase advance belonging to a full turn:

$$Q = \frac{1}{2\pi} \oint \frac{\mathrm{d}s}{\beta(s)}$$

What happens if the tune of a ring is 1/2 (or any integer divided by 2) and one extra quadrupole is added to the setup with tiny quadrupole strength at any point s? Since the effect of this quadrupole is not considered in the precalculated beta function, the particles suffer a small kick in the normalized phase space with each passage.

The track of a single particle in consecutive turns is visible in Fig. 3.8. Since it arrives each turn in the same phase or rotated by π it always gets kicked in the same direction. The same effect happens, if any of the magnets has a tiny quadrupole field component which was not accounted for (more on gradient error in [13]). This effect is called the quadrupole (or second order) resonance and results in a growing beta function (blowing up the beam).

It is impossible to avoid imperfections, so resonant tunes must be avoided.

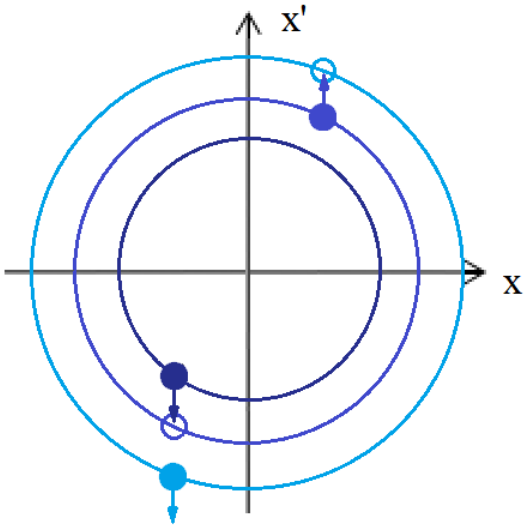

Figure 3.8: Effect of a quadrupole error to a particle with tune i/2

There are higher order multipole resonances (e.g. third order resonance) causing the same issue, but the impact of them decrease with the order of the resonance (since $B_y \sim x^{n-1}$, and $x \ll 1$). When both the horizontal and the vertical phase spaces are taken into account, the general aim is to avoid the resonance condition:

$$nQ_x + mQ_y = N$$

where Q_x and Q_y are the horizontal and vertical tunes, respectively, and n, m and N are integers. The critical Q_x,Q_y values and a somewhat safe working point is visible in Fig. 3.9.

So far only on-momentum particles were discussed. These are the particles that have longitudinal momentum equal to the nominal momentum used to calculate the beta function, and the tune. In reality, there is always some finite momentum spread, which causes so-called chromatic aberration.

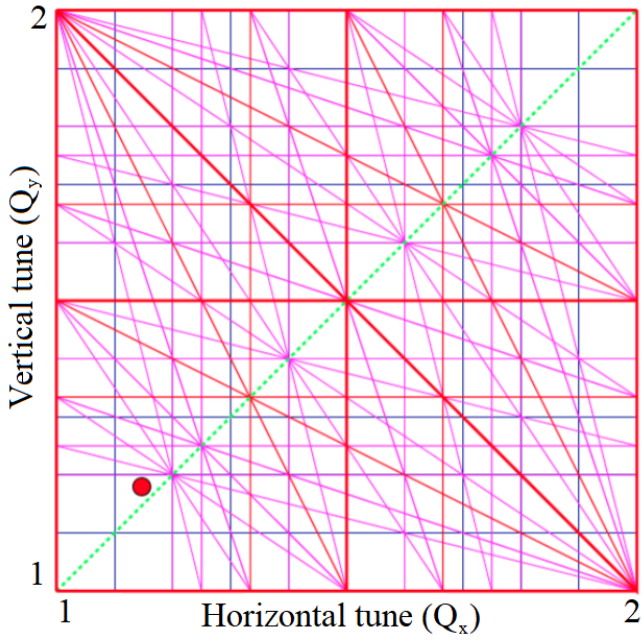

Figure 3.9: Tune plot showing the critical Q_x, Q_y values, taken from [13].

Chromatic aberration (or chromaticity) is introduced in accelerator physics similarly to optics (a detailed discussion of chromaticity can be found in [14]). In optics rays with different wavelength suffer different deflection on a lens, so their focal points are offset from each other. The analogy to this is that the longitudinal momentum spread causes different particles to have different (quadrupole) focal lengths (shown in Fig. 3.10.), and as a consequence change the tune slightly for off-momentum particles. The chromaticity is defined as the variation of the tune with the relative momentum deviation:

$$Q' = \frac{\mathrm{d}Q}{\mathrm{d}\delta},$$

where $\delta = \frac{\Delta p}{p_0}$.

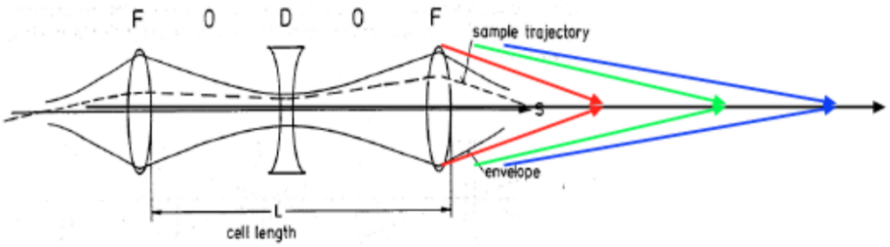

Figure 3.10: Effect of chromatic aberration in a FODO lattice.

In a ring with strong focusing quadrupoles, the chromaticity is always negative. Sextupole magnets have to be used to reduce chromatic aberration (the explanation of this effect is beyond the scope of this work). In short, sextupole magnets can be treated as x- or y-dependent quadrupoles, and therefore correcting sextupoles are typically placed at locations where the value of dispersion

is large, i.e. where particles with different momenta are separated in the transverse plane (more on dispersion in [9]).

If chromaticity was not corrected in the LHC, it would be ~ 250 (unitless). With momentum spread $\delta = \frac{\Delta p}{p_0} = \pm 0.2 \cdot 10^{-3}$ the tune that the particles see would range from 0.13 to 0.43 meaning that the spot on the tune plot would overlap with several critical lines. The beam would be unstable due to the multipole resonances.

Sometimes, however, inducing a resonance is necessary. One of the most important examples of this is the third order resonance driven slow extraction used in SPS.

4

Extraction from a synchrotron

In this chapter, we summarize the possibilities of extracting beam from a synchrotron, most of the material covered here can be found in more detail at [15], and discuss slow extraction in detail, in order to see the difficulties and possible enhancements to increase its efficiency.

4.1 Fast extraction

There are two main devices used to make fast extraction from a high energy synchrotron possible. The kicker magnet, which is simply a quickly rising weak dipole magnet, and the magnetic septum, which is a device that separates a high field region from a zero-field region. The nominal trajectory typically traverses the zero-field region. An example septum magnet is visible in Fig. 4.1.

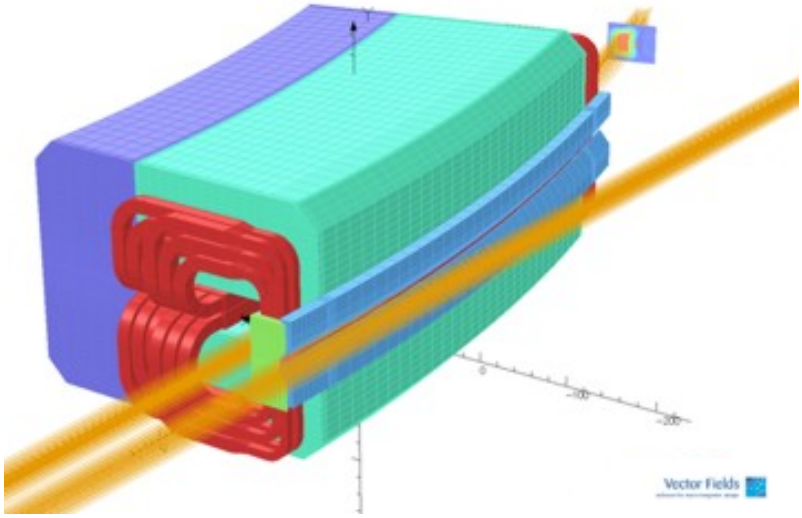

Figure 4.1: Illustration of a septum magnet. The blue part between the circulating (right) and extracted (left) beam is the septum blade. Image taken from [16].

The complete extraction procedure is as follows:

- First a set of slowly rising so-called closed orbit bumper magnets are ramped up so that the orbit of the circulating beam is closer to the septum. They are called closed orbit bumpers

because they only affect the section of the beam between the first and the last closed orbit bumper. In some extraction schemes, bumpers are not necessary or feasible to use.

- Then a quick rising magnetic (or at low energy electrostatic) kicker sends the whole beam slightly off-track.
- After some drift (so that the beam gets further away from the nominal trajectory) the beam enters the high field region of the septum magnet, that drives the beam away from its original position.
- The extracted beam enters a separate beampipe and can be dealt with separately (steering towards its destination, or dumping).

During this process, the beam gets further away from the closed orbit step by step. The kicker is needed to create space for the magnetic septum blade (which separates the low field and high field regions). The magnetic septum is needed because the kicker is a weak magnet (in order to be as fast as possible). After the septum magnet, the extracted beam is far enough, so that its beampipe does not interfere with the next dipole magnet of the circulating beam. A usual setup of extraction is visible in Fig. 4.2. The same setup (with reverse ordering) can be used for injection.

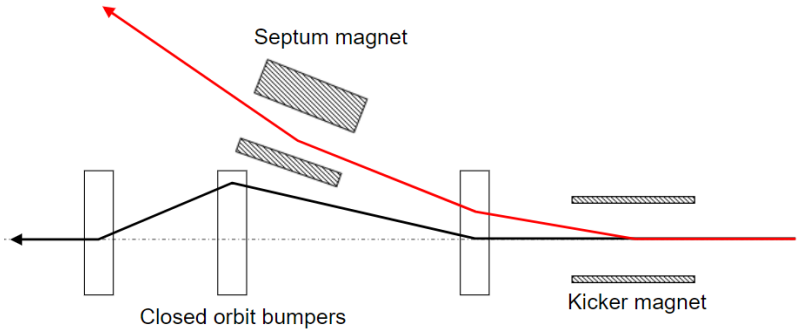

Figure 4.2: Concept of the fast extraction.

4.2 Multi-turn extraction

The main difference between single turn and multi-turn extraction is that in multi-turn extraction no kicker magnet is used. Instead, the beam is “cut” somehow by the septum (as shown in Fig. 4.3.). However, the septum blade cannot be thinner than a few millimetres. If the beam was swept slowly through the blade, all the particles would be lost (that is why the kicker needs to be quick in single turn extraction).

Instead of a magnetic septum, an electrostatic septum is used whenever the thick septum blade is not acceptable. It is a device which has a long plain cathode, and several thin wires (or sometimes a thin foil) as the anode separating the high and the zero-field regions. In the case of the SPS one electrostatic septum (called ZS in the remaining of the work) is 3.1 m long with 2080 stretched wires at 1.5 mm spacing (seen in Fig. 4.4.). The slow extraction setup contains five ZS to steer the

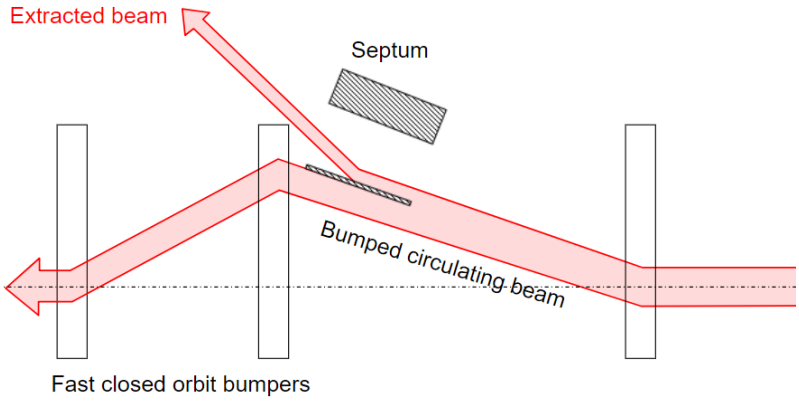

Figure 4.3: Concept of multi-turn extraction.

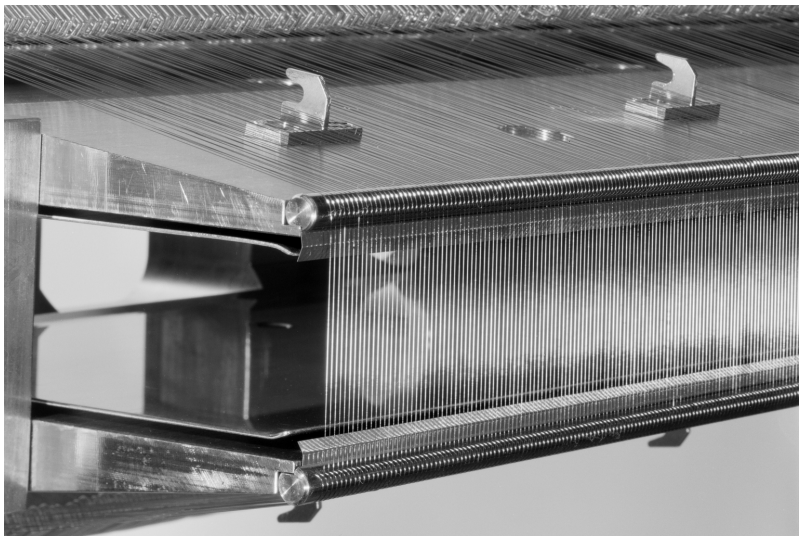

Figure 4.4: Picture of the ZS. Behind the wires is the circulating beam's trajectory, the zero-field region. The cathode is not presented in the picture.

extracted particles far enough from the circulating orbit. The wires are 25 μm thick in the first two ZS, and 50 μm in the last three, and they are all made out of tungsten-rhenium (W74Re2).

Beyond the electrostatic septa, there are 3 thin and 5 thick magnetic septa in the slow extraction system (MST and MSE) as well as a protection device (TPST) before MST. The whole setup is visible in Fig. 4.5. Two quadrupoles are not marked in the figure (one defocusing between the last ZS and TPST, and one focusing between MST and MSE).

In Fig. 4.5. it is also visible that the design orbit (red line in the middle of red stripe) has a 45 mm offset from x=0. This 45 mm is the bump distance at the upstream end of the ZS caused by the closed orbit bumpers.

4.3 Sextupole driven slow extraction

In the case of a slow extraction (discussed in detail in [17]), the number of turns necessary to extract the beam can be really large. In the SPS slow extraction it is $\sim 2 \cdot 10^5$ turns. For the concept

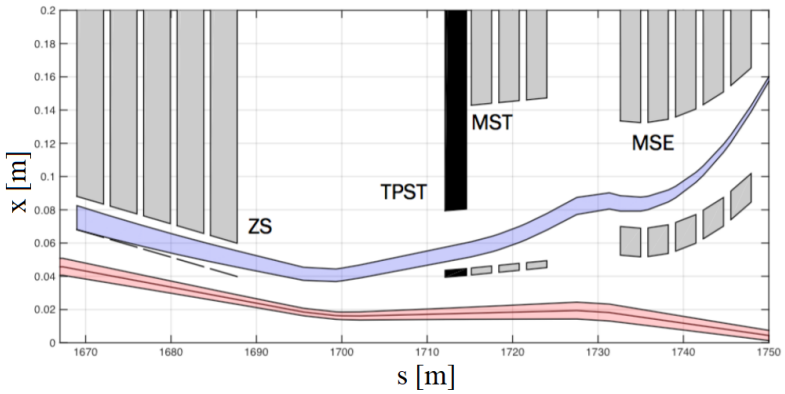

Figure 4.5: Setup of the SPS slow extraction. The setup is similar to a simple multi-turn extraction. Image taken from [17].

to work the beam has to be huge in the position of the ZS. To understand why, let's assume an extraction efficiency of 50% which means that the part of the beam outside the ZS wires has to be at least as thick as the ZS wires ($\geq 25\ \mu\mathrm{m}$). So every turn the wires extract $25\ \mu\mathrm{m}$ of the beam, while another $25\ \mu\mathrm{m}$ is lost due to scattering on the wires. This would mean that the beam has to have a diameter of $d = (25\ \mu\mathrm{m} + 25\ \mu\mathrm{m}) \cdot 2 \cdot 10^5 = 10\mathrm{m}$. Of course, this is not possible, that is why instead of increasing the whole beam size, the third order resonance is induced.

The tune of the stable circulating particles is a little below 1/3 integer (in the SPS $Q_x \simeq 26.6$), and at the beginning of the slow extraction, the tune is slowly changed in the direction of the exact resonance (in the SPS 26.66666667). This starts the effect visible in Fig. 4.6. in which particles outside of a triangular separatrix become unstable, and move away from the rest of the beam turn by turn.

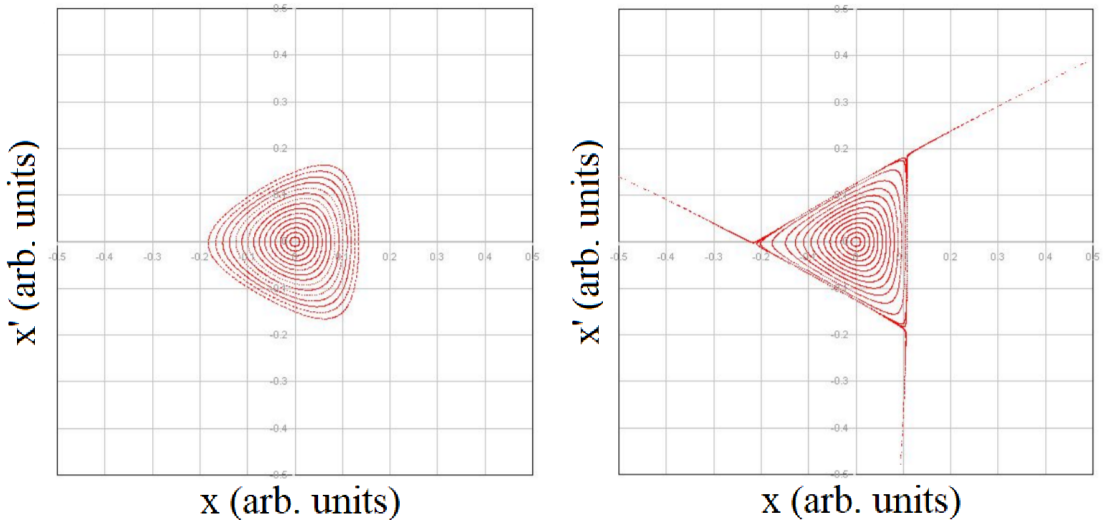

Figure 4.6: Normalized phase space plot of the third order resonance. Beam on the left is stable (inside the separatrix), while the outer particles of the beam on the right are outside of the separatrix, and unstable. Image taken from [17].

Particles which are on one arm of the separatrix in one turn will be on the counterclockwise

rotated arm in the next turn. Particles return to the same arm every three turns, but always a little further from the middle than earlier. If we track the phase space position of one unstable particle it seems like if it were "walking" outwards with increasing steps.

The so-called spiral step is an important parameter of the slow extraction. Assume a particle which is just barely on the circulating side of the wires in one turn, then three turns later it is the extracted particle which is furthest away from the origin. The difference between the particle's x coordinates in this turn and 3 turns later is called the spiral step. In other words, this is the length of the section on which particles are extracted or lost.

The particle density (spatial density in x) is heavily reduced in the separatrix arm (if the change of the tune is slow enough), so $1/(2 \cdot 10^5)$ part of the beam is distributed to ~ 10 mm, the spiral step. The ZS extracts this 10 mm section, while particles are scattered on the wires only from the ~ 25 μm long section of the separatrix arm. As a consequence the efficiency increases to $\sim 94 - 95\%$.

The normalized acceptance plot of the ZS is visible in Fig. 4.7. The red vertical line on the left is the phase space region in which particles would hit the ZS wires from the front. The dark purple region on the right represents particles which would hit the cathode from the front. Particles which are in the bright red phase space region would hit the ZS wires from the side (up left - hit from circulating side, bottom right - hit from extracted side). Particles in the bright purple area hit the cathode from the side. Particles in the green area are extracted (at least they do not hit ZS itself).

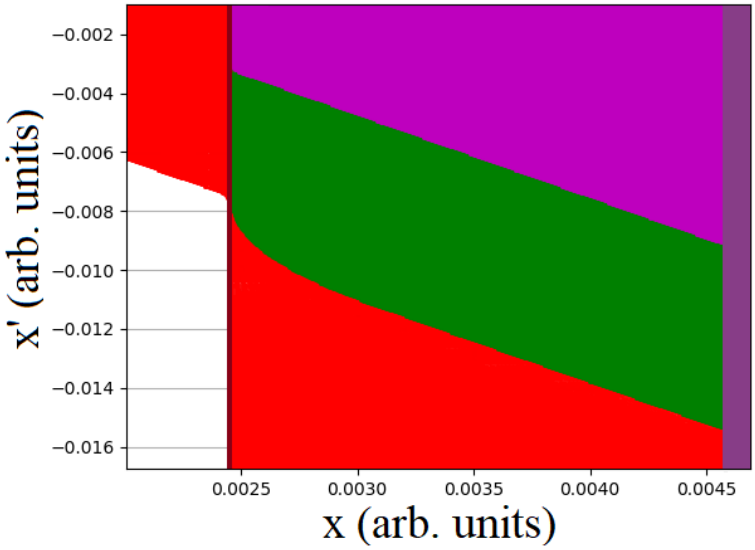

Figure 4.7: Acceptance plot of the ZS. Particles in the dark red region hit the wires frontally, bright red region represents particles that hit the wires from one of the sides. Dark purple particles hit the cathodes frontally, while bright purple ones hit it from the side.

The arm of the third order resonance has to cross the thinnest section of the red region. This can be achieved by aligning the ZS so that it has the same angle as the particles which hit it from the front. In all the phase space plots in this work a simplified version of this acceptance will be visible, as in Fig. 4.8. which shows a typical extraction. Green dots represent extracted particles,

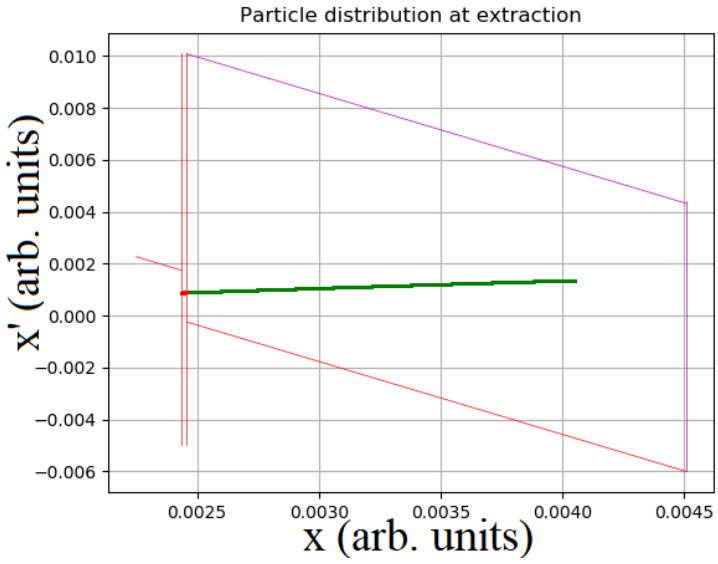

Figure 4.8: Extraction plot of the slow extraction. Green particles are extracted, red particles are lost on the wires.

while red dots represent the lost particles (circulating particles are not shown).

In the SPS so-called chromatic extraction is used, which means that during the slow extraction the chromaticity of the beam is non-zero. As discussed above if chromaticity is finite, particles with different momenta see a different tune. This way different momenta particles are becoming unstable at different on-momentum tune. This makes the extraction "smooth", the spill more continuous. As a side effect, the average momentum of the spill depends on time.

4.4 Possible enhancements

The particles which are scattered on the ZS wires are lost on the protection devices (e.g. TPST between ZS and MST). The activation of these pieces of equipment gives a limit to the number of protons extracted. Increasing the number of protons-on-target would increase the activation if no efficiency enhancement is applied. There are a few ideas considered that would reduce the losses (so increase the efficiency) of the SPS slow extraction.

4.4.1 Diffuser

The first concept is to use a so-called passive diffuser. A diffuser is installed upstream from the ZS, and its goal is to reduce the particle density hitting the electrostatic septum wires. The passive diffuser, studied in [18], achieves it by scattering the part of the beam which would hit the wires. In the SPS it is achieved by having a line of 20 thick Tungsten-Rhenium, or Tantalum wires ($\sim 150 - 200\ \mu\mathrm{m}$) on which the particles are scattered slightly (they get a small random x' kick). This particle distribution is rotated in normalized phase space and by the time it arrives to the ZS

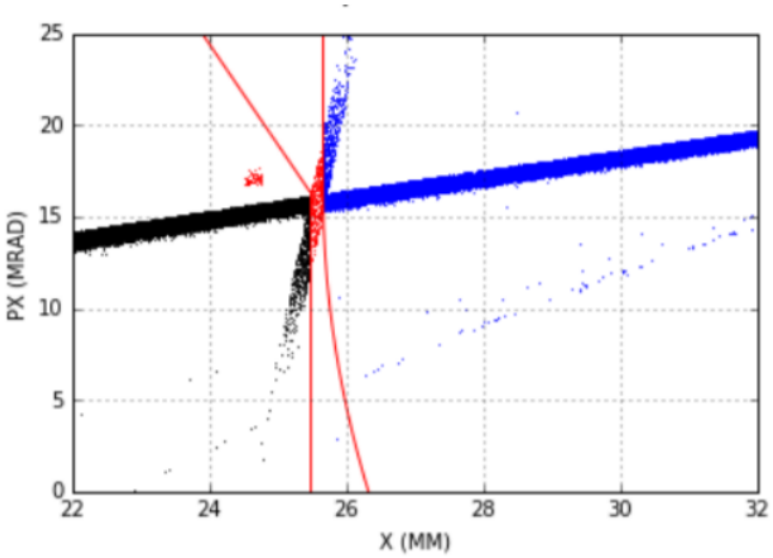

Figure 4.9: Particle distribution at the ZS if the diffuser is installed upstream from the ZS. The red lines represent the region where particles hit the wires, and are lost due to scattering. Black, red and blue particles are circulating, lost and extracted, respectively. Image taken from [18].

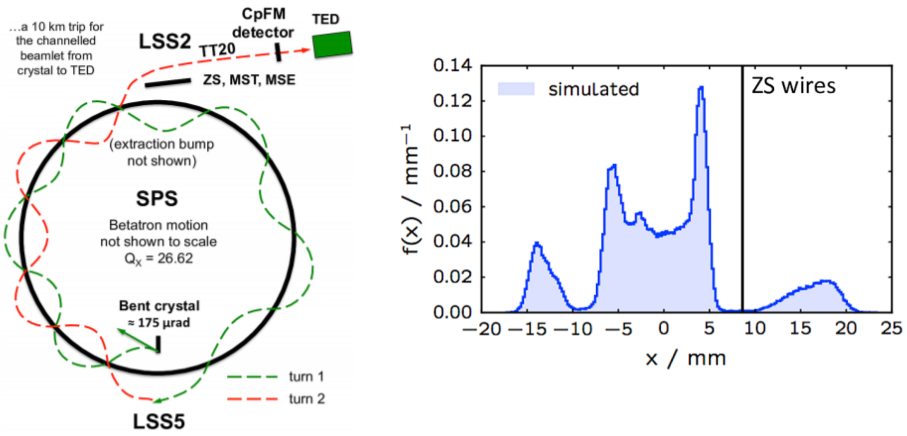

Figure 4.10: Bent crystal assisted extraction scheme and the simulated particle denisty at the ZS wires. Images taken from [19].

the particles scattered on the diffuser appear as reduced particle density on the ZS wires (as seen in Fig. 4.9.).

The diffuser installed in the SPS in February 2018 was designed and constructed by our research group at Wigner Research Centre for Physics (Budapest) and Engious Ltd. (Székesfehérvár).

The first tests have been done and so far the diffuser seems to be working as expected. The simulations predict a possible loss reduction of 10-20

It is an ongoing study to use bent silicon crystals to prepare a particle distribution at the ZS position which has minimal particle density at the wires (discussed in [19])(this is also called an active diffuser). The schematic of the crystal assisted extraction and the simulated particle density as a function of x can be seen in Fig. 4.10

Both the active and the passive diffuser uses the “shadow” of an object to reduce the particle

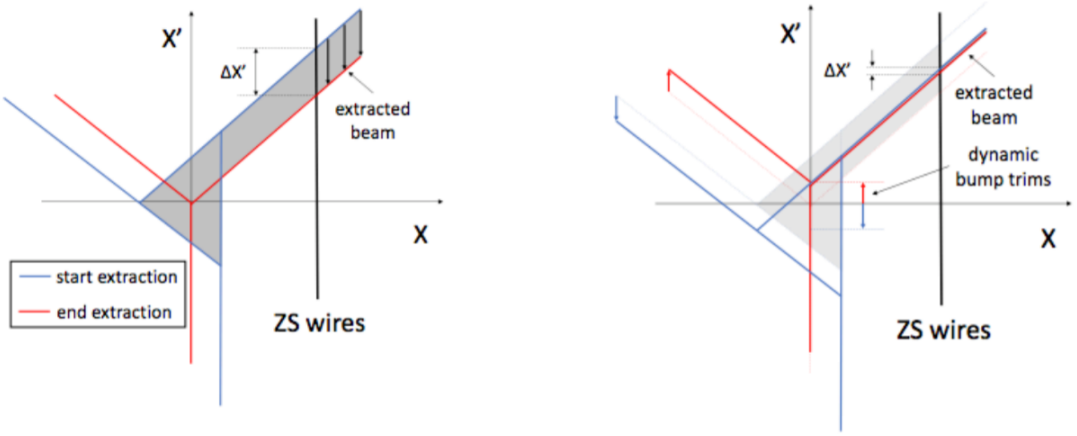

Figure 4.11: Concept of the dynamic bump. Image taken from [20].

density at the wires.

4.4.2 Dynamic bump

As the tune gets closer to exact resonance (or the sextupole magnet strength is increasing) the separatrix of the third order resonance is shrinking. This causes the arm to move in phase space, consequently, the point where the arm crosses the ZS wires is changing. As seen in Fig. 4.7. the ideal crossing region is small, so this effect increases the "effective septum thickness".

The dynamic bump, studied in [20], is aimed to reduce the x' spread of the extracted particles during the spill, by changing the closed orbit bumper's strength slowly during the extraction. The concept is visible in Fig. 4.11.

Dynamic bump is the most effective in combination with one of the other loss reduction concepts.

4.4.3 Phase space folding

The third concept is to fold the separatrix arm in a way, that there are more particles in the extraction gap, while less hitting the wires (as seen in Fig. 4.12.). In theory, this can be achieved by using higher order multipole magnets (studied in [21]), but the magnet strength needed to increase the efficiency by a significant amount is at the moment too high for the method to be feasible.

Another way to achieve the same effect is to fold back the separatrix arm using a massless septum (discussed later) so that it stays further from the cathode, as seen in Fig. 4.13. Space which is freed up can be used by increasing the sextupole magnet strength and this way increasing the spiral step. The increased spiral step causes lower particle density at the wires so in the end increases the efficiency.

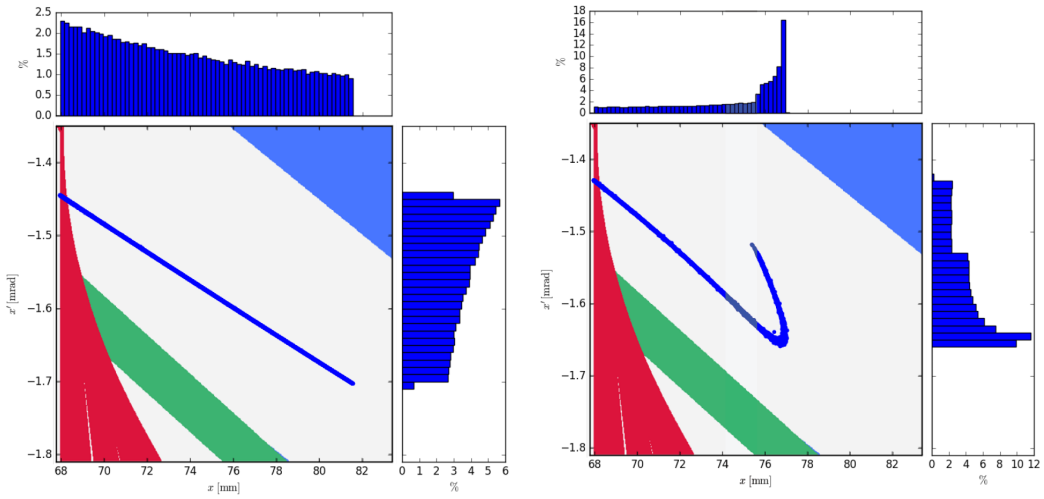

Figure 4.12: Phase space folding using higher order multipole magnets. Extraction plot of original (left) and folded (right) case, and the histogram of particle positions. Images taken from [21].

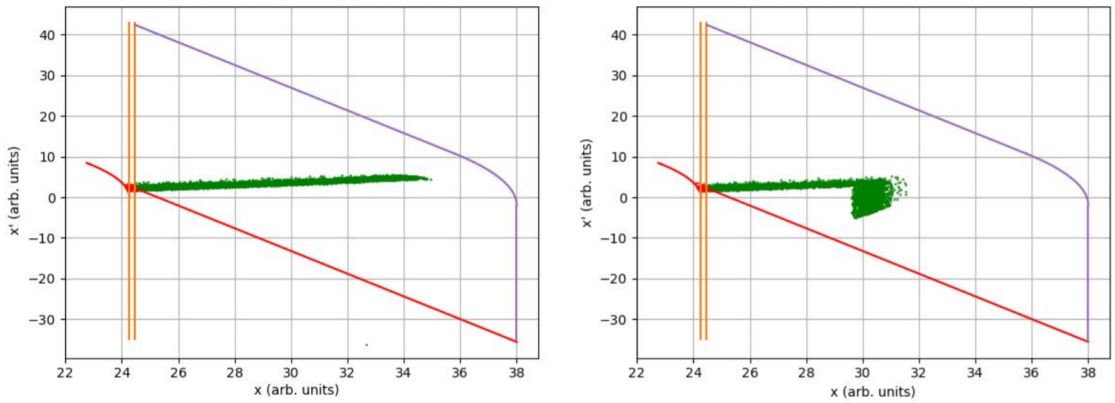

Figure 4.13: Original (left) and folded(right) separatrix arm extracted.

5

Massless septum

A septum is a device which has a high and a low (usually zero) field region and separates the two with the septum blade. A massless septum is a device that creates high field gradient between the two regions without any material in between them. The high gradient transition zone is called the transverse fringe field. The transition is of course not as sharp as for a regular septum.

An example massless septum design and the field as a function of the horizontal coordinate is visible in Fig. 5.1. This design of a massless septum was studied in [22] in order to check the feasibility of a different extraction method.

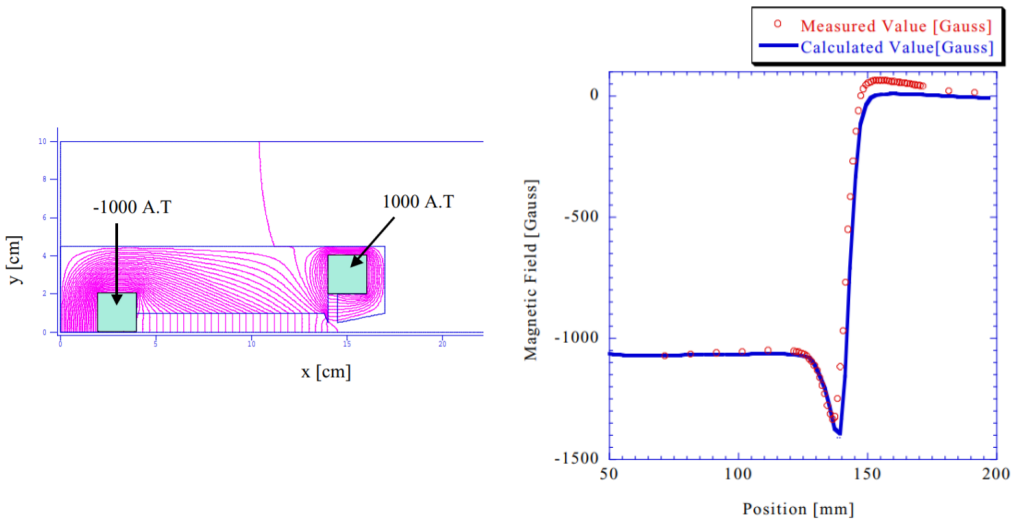

Figure 5.1: Design of a massless septum studied in [22] (left) and the magnetic field of it (right).

Massless septa are rarely used in accelerator physics because the usual goal of a septum is to minimize the length of the transition region between low and high field, and a massless septum fringe field length is usually much larger than the width of a septum blade.

The other issue with massless septa is that the field homogeneity is usually much worse in the low field region than in a regular septum (leakage field is visible in Fig. 5.1.). There are usually really strict requirements on the quality of the zero field region since the circulating particles traverse this region multiple times, and field errors can lead to instabilities, as discussed earlier.

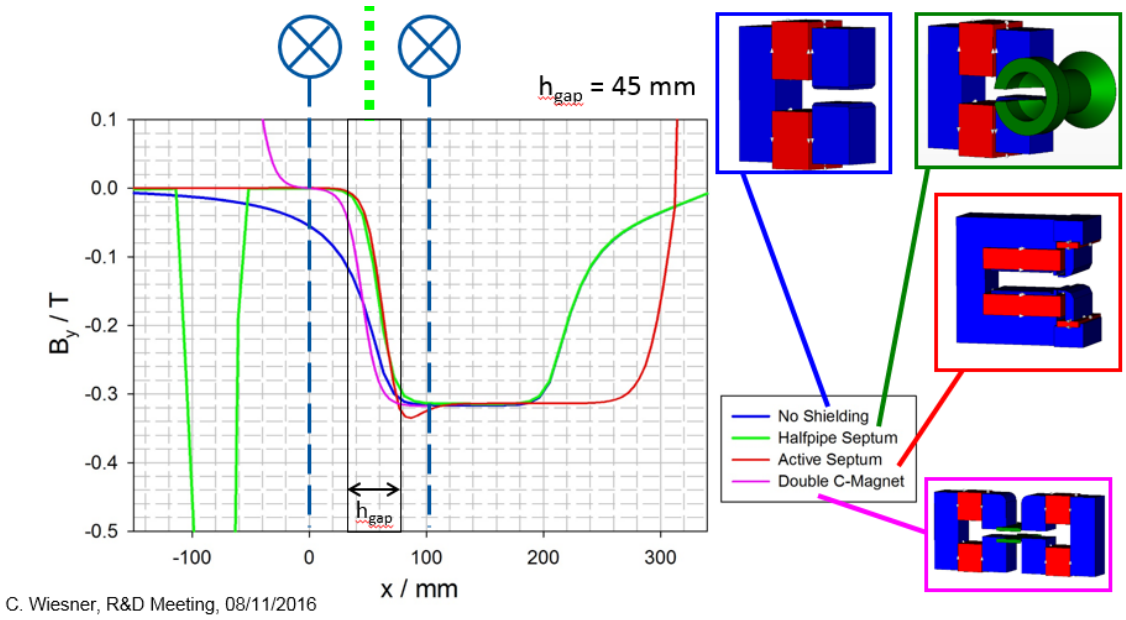

Figure 5.2: Some example massless septum designs, and their corresponding magnetic field.

A few other example massless septum designs and their corresponding magnetic field is visible in Fig. 5.2.

5.1 Method of phase space folding using a massless septum

The idea is to use the fringe field of a massless septum (the transition region between high and low field) to fold back the separatrix arm. In my simple proof of principle simulations, I used a massless septum with a linear fringe field (meaning linear kick also, as seen in Fig. 5.3.).

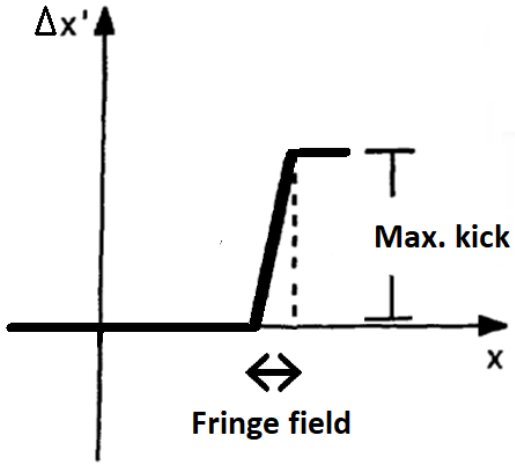

Figure 5.3: Simplefied massless septum with linear fringe field.

Since the high field region is not used at all, we can think of the massless septum as having a zero field region and a high gradient linear fringe field. This solves one of the issues with massless

septa in general, namely that the fringe field width does not have to be minimized.

After the kick by the massless septum the affected separatrix arm will look like in Fig. 5.4. Notice that the angle of folding can be tuned by changing the fringe field gradient.

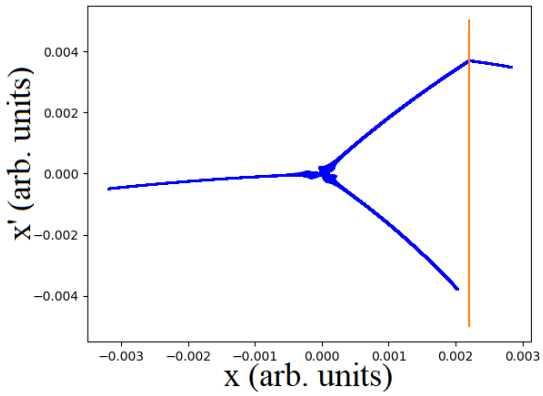

Figure 5.4: Separatrix of the third order resonance affected by a massless septum kick.

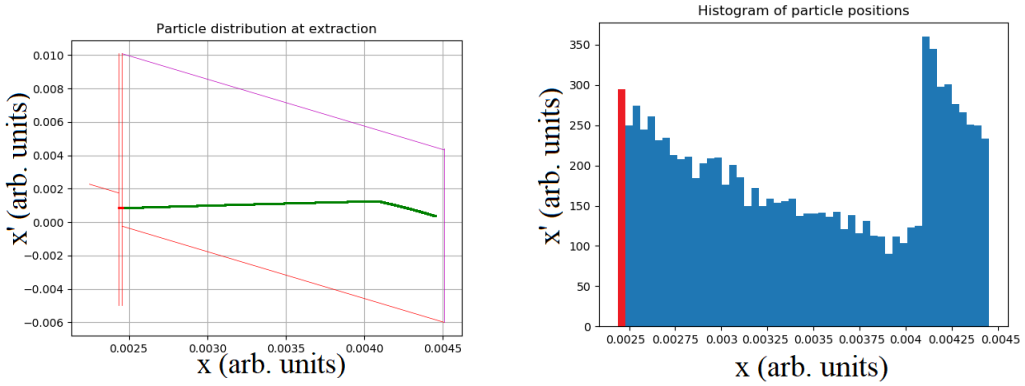

Figure 5.5: Extraction plot of a folded third order resonance arm (left), and the histogram of lost and extracted particle positions (right).

The effect of the kick on the phase space distribution at the ZS can be seen in Fig. 4.13. The freed up extraction space can be used by increasing the spiral step (by increasing the sextupole strength), and in parallel by changing the position of the massless septum. The result is visible in Fig. 5.5. The histogram shows the extracted (and lost) particle densities.

6

Simulation method

All the simulations were written in python. Since this is a proof-of-principle study to see if the concept works at all, and to check the limitations, using a simple programming language like python was much more reasonable than to write the simulation in MAD-X (which is one of the standard simulation tools used for accelerator design at CERN).

The code is essentially a particle tracking routine which evolves 10000 particles' normalized phase space position around a defined ring, which consists of some devices (sextupole magnets, massless septum, ZS), and a given phase advance rotation between them. A full simulation consists of 5000 turns.

In the simulation chromatic effects are completely neglected. This means that instead of chromatic extraction (used in SPS) the so-called amplitude extraction is used. As the tune is approaching the exact resonance the separatrix triangle is shrinking, so the "outer" particles are extracted first.

Since the beta function of the SPS is known, particle tracking between any two points of the unmodified linear ring lattice can be done by rotations in normalized phase space. The effects of the sextupoles, the massless septum and the ZS were implemented as discrete operations in the horizontal phase space (x, x'), as described below:

- The sextupole magnet applies a quadratic kick to the particle's normalized momentum

$$\Delta x'_s(x) = S \cdot x^2,$$

  where S is the sextupole strength.

- The massless septum kick is also a thin lens kick:

$$\Delta p_{ms}(x) = \begin{cases} 0, & \text{if } x < a \\ g \cdot (x - a), & \text{if } a < x < b \\ g \cdot (b - a), & \text{if } b < x \end{cases},$$

  where a and b are the two "edges" of the fringe field, and g is the integrated gradient of the fringe field.

- The ZS is simulated as several (30) thin slices. The reason for this is that the full length of the ZS ($\sim 17\mathrm{m}$) is equal to $0.0546 \cdot 2\pi$ phase advance, so thin lens approximation is not appropriate to use. In each slice the wire's position is different in the normalized phase space due to beta changing.
  - The particles which are hitting the wires or the cathode are taken out of the system. There was no scattering simulated.
  - Particles which are between the wires and the cathode (extraction gap) receives an upwards kick from the electrostatic field, and proceed to the next slice.
  - Particles which are on one side of the wires in one slice and the other side in the next slice are considered lost.
  - If a particle is in the extraction gap of the last slice, it is marked as extracted.

The simulation makes it possible to find the required massless septum parameters (starting position of the fringe field, and fringe field gradient) for a given sextupole strength so that the number of lost particles is minimal.

The code was validated against MAD-X and a separate python simulation using the same parameters.

7

Studies

Two studies were done, the first of which was a preliminary study of the concept itself, it was done mainly in the summer of 2017 as a CERN summer student project, the second one was aimed to check the possible efficiency increase in the case of SPS slow extraction, and was done in the spring of 2018.

There are some minor differences between how the two simulations were set up, all of which play a role in getting different efficiency enhancement results.

The most trivial difference between the studies comes from the setup of the ring. In the first one, the simulation had one sextupole magnet only and the massless septum was right after the sextupole (no phase difference). The distance between the sextupole and the ZS is a parameter to optimize for.

In the second simulation, most of the setup parameters were taken from the real machine. First and foremost there are 4 extraction sextupole magnets used in the SPS. In the simulation, the strength of these 4 sextupoles, and their longitudinal position (s) is equivalent to their real counterparts. The ZS's parameters (s position and bump) are also taken from the SPS design. This means that the phase difference between the last sextupole and the ZS is fixed, so the only variable parameters are the s position of the massless septum.

Another difference between the studies is that in the first the used acceptance plot was slightly different from the real ZS acceptance. The change of the beta function inside the ZS was neglected (which was a mistake, but did not change the results significantly).

While these few differences have visible effects on the extraction plot, they do not change the achievable efficiency. However, in the first study, the tune was set to be $1/3$ and the sextupole strength was positive, while in the SPS (and also in the second study) it is 26.6666 (which in rotational terms is equivalent to $-1/3$), and the sextupole strength was negative. These two differences flip the separatrix around the vertical axis. At first glance, this does not seem to be a problem, but it turns out that at high sextupole fields the arms of the separatrix become nonlinear. This nonlinearity can be seen in Fig. 7.1.

The different tune, and sextupole strength results in different bending directions of the extracted arm. In the first case, the arms are bending counterclockwise, while in the SPS simulation they are bending clockwise. The result of this is that after the massless septum kick in the second simulation

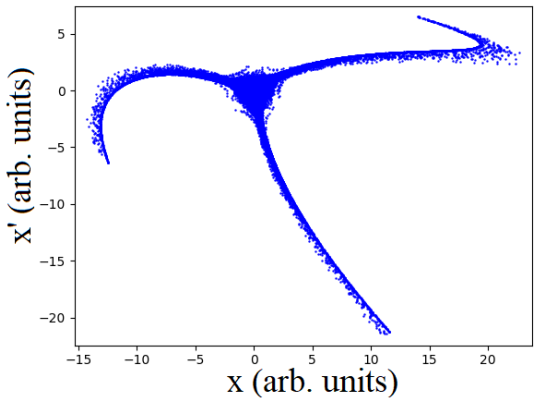

Figure 7.1: Nonlinearity of the separatrix arms at high sextupole fields.

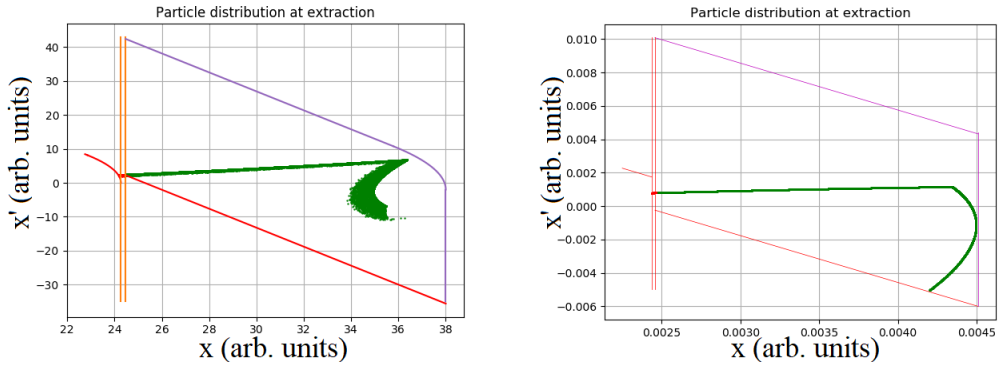

Figure 7.2: Extraction plot of the first (left) and the second (right) study, showing the different bending directions of the separatrix arm.

it is much harder to fit the beam into the acceptance (even though the nonlinear effect in the SPS is much less significant due to the sextupole kick being divided into 4) as seen in Fig. 7.2 This gives an upper limit to the sextupole strength.

The tune is changing from below the resonance to slightly above it in the first study, while it is kept intact at exact resonance in the second one. This is why the arm's "thickness" is reduced in the second simulation (like if dynamic bump was used) as also seen in Fig. 7.2.

The integrated sextupole strength is parametrized as $S = S_{fact} \cdot S_0$, where S_0 is the original sextupole strength that results in an extraction plot similar to the one simulated by MAD-X SPS simulations. This way the sextupole kick can be written as $\Delta x' = S_{fact} \cdot S_0 \cdot x^2$. The extraction efficiency is studied as a function of the strength factor, S_{fact}.

On the axes of the figures, it is visible that in the first study not the original normalized coordinates were used (they are "scaled" in both dimensions by $\sqrt{\beta}$), but this difference only plays a role in the representation of the particle distribution. In the second study the "real" normalized coordinates are used (transformation to and from real coordinates shown above).

8

Results and discussion

8.1 First study

As explained before, the first study was aimed to provide information about the concept itself. How does the efficiency grow with sextupole strength? What are the limitations? In order to acquire the answers to these questions, the massless septum parameters were optimized for each sextupole strength factor in the region 1-5 increasing by half steps. Each case is optimized through the tuning of three parameters:

- The massless septum's integrated fringe field gradient (g),
- The massless septum's x position,
- The phase difference between the sextupole magnet and the ZS (there is no phase difference between the sextupole magnet and the massless septum in this study).

8.1.1 $\mathbf{S_{fact}} = 1$

In this study the normalized sextupole strength is $S_0 = 0.02$. As a result, the extraction plot is similar to the extraction plot of a more realistic MAD-X simulation. The extraction plot and the histogram of extracted and lost particles at $S_{fact} = 1$ can be seen in Fig. 8.1.

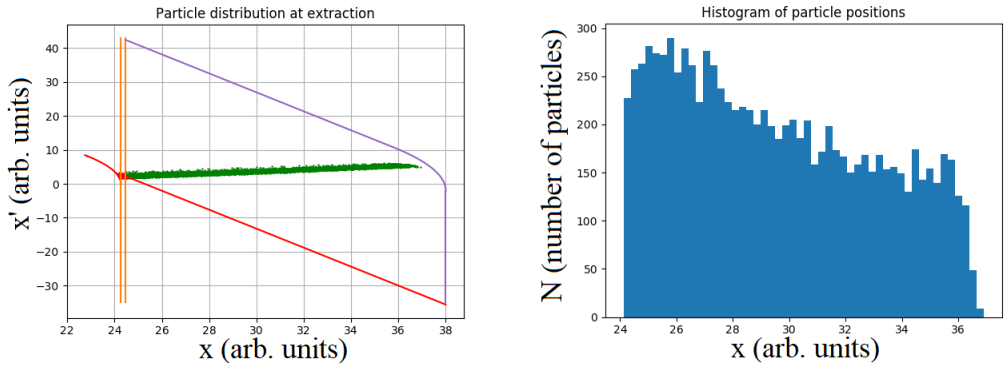

Figure 8.1: Extraction plot and histogram of the particles at $S_{fact} = 1$.

The number of lost particles, in this case, was N_l=349, while N_c=389 were not extracted from the full set of N_0=10000 particles and remained circulating in the ring. N_c is decreasing as the sextupole strength goes up. The reason for having stable particles is that the tune is changing too quickly for the inner particles to become unstable. These particles are not counted in the analysis. The number of extracted particles is $N_e = N_0 - N_l - N_c$, and the efficiency of the "baseline" case is then: $\eta = \frac{N_e}{N_0 - N_c} = 0.9637$.

The number of lost and stable particles and the efficiency of the following cases will be summarised at the end of the section.

8.1.2 $\mathbf{S_{fact}} = 2$

If the strength factor is $S_{fact} = 2$ the massless septum needs to have a negative fringe field gradient with absolute value $|g| = 3.45$ at least. If $|g|$ is lower than that, then some particles will hit the cathode. Note that as long as the arm is folded enough so that it does not hit the cathode, and not "overfolded" so that it does not hit the wires from the extracting side, the extraction efficiency is unaffected by the massless septum parameters (position, and fringe field gradient). This leaves a lot of room for the shaping of the extraction profile. An example extraction profile ($g = -3.778$) is visible in Fig. 8.2.

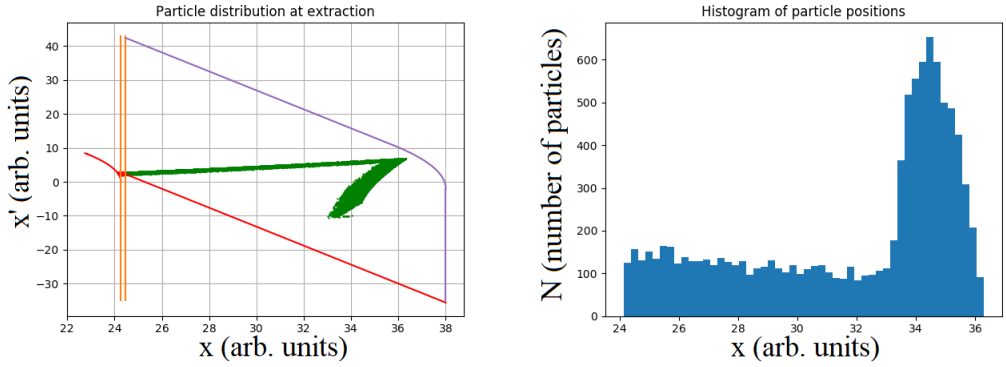

Figure 8.2: Extraction plot and histogram of the particles at $S_{fact} = 2$.

8.1.3 $\mathbf{S_{fact}} = 3$

In this case, the nonlinearity of the arm is becoming significant. The massless septum needs to have a fringe field gradient with absolute value at least $|g| = 4.06$. An example extraction profile with $g = -4.167$ can be seen in Fig. 8.3.

8.1.4 $\mathbf{S_{fact}} = 4.5$

This is the highest possible strength factor achieved with low losses. The limitation is the nonlinearity of the separatrix at high sextupole fields. The separatrix bends back on itself and is also folded by the massless septum, which causes the double folded structure of the extraction plot seen in Fig. 8.4.

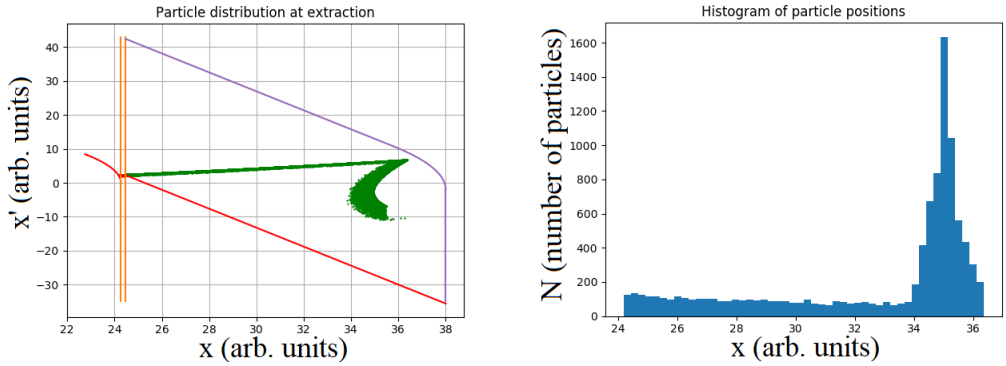

Figure 8.3: Extraction plot and histogram of the particles at $S_{fact} = 3$.

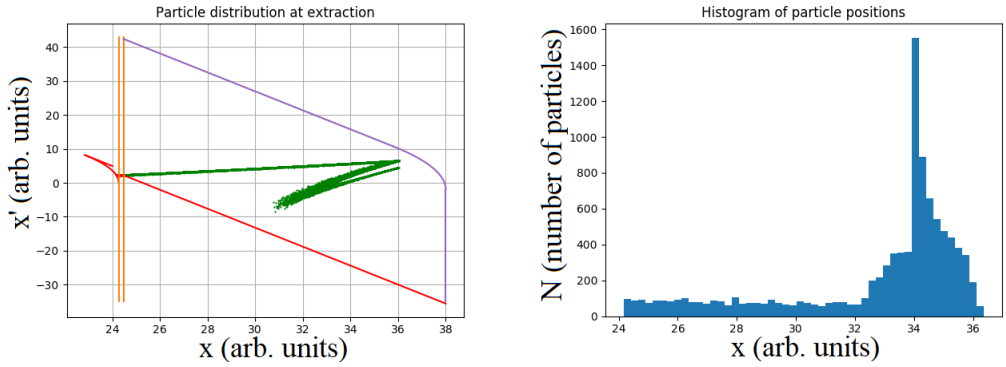

Figure 8.4: Extraction plot and histogram of the particles at $S_{fact} = 4.5$.

As the sextupole strength increases further the nonlinearity gets out of control and it becomes impossible to keep the losses low. The field gradient was $g = 5.176$ in the example seen in Fig. 8.4.

8.2 Conclusion of the first study

The summary of the achieved efficiencies and the number of lost and extracted particles can be seen in Table 8.1. The number of lost particles and the efficiency as a function of the sextupole strength factor can be seen in Fig. 8.5.

Table 8.1: Results of optimization in the first study.

Field strength	Wires	Extracted	Remaining	Efficiency
0.02	349	9262	389	0.9637
0.03	305	9512	183	0.9690
0.04	183	9719	98	0.9815
0.05	176	9765	59	0.9823
0.06	156	9801	43	0.9843
0.07	147	9824	29	0.9853
0.08	141	9837	22	0.9859
0.09	105	9868	27	0.9895

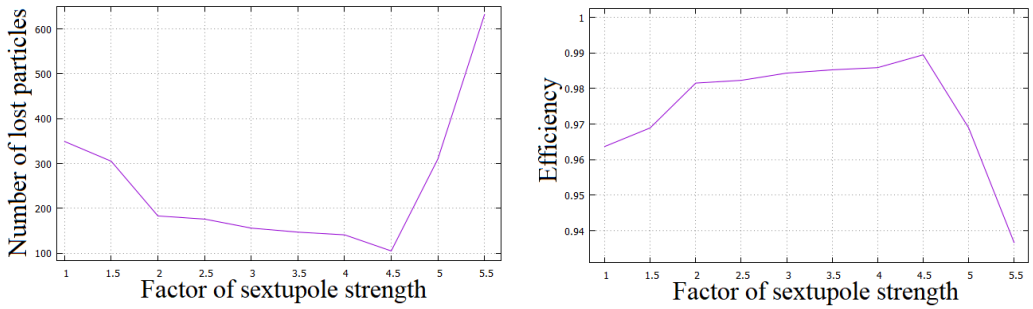

Figure 8.5: Number of lost particles (left) and the efficiency of the slow extraction (right) as a function of the strength factor in the first study.

The results clearly show that the concept is working. The extraction efficiency increases from 96.4% to 99%, which means that the losses (and thereby the activation of the surrounding materials) decreases by a factor of 3.6 for the same number of extracted particles, or the number of extracted particles can be increased by the same factor if the same activation level is kept. As a byproduct of the increased sextupole field, the arm of the resonance becomes thinner. However, this does not increase the efficiency directly.

The limitation is clearly the nonlinearity of the separatrix arms at high sextupole field. Figure 8.6. shows the distortion of the separatrix at $S_{fact} = 6$.

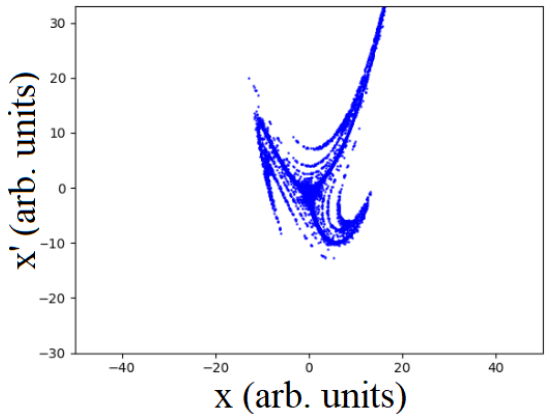

Figure 8.6: Nonlinearity of the separatrix arms at $S_{fact} = 6$.

To get a feeling of the feasibility of a massless septum field needed to achieve such loss reduction, the largest field gradient and the maximum field of the corresponding massless septum was calculated in real units. The integrated maximum field of the septum used in the case $S_{fact} = 4.5$ is $0.66\ \mathrm{Tm}$, this corresponds to a $500\ \mu\mathrm{rad}$ kick. The integrated fringe field gradient of this massless septum is $0.078 \frac{\mathrm{Tm}}{\mathrm{mm}}$. A massless septum with these parameters could be achievable, although not straightforward to design.

8.3 Second study

The second study was aimed to be a bit more realistic than the first one, as described in detail above. The code needed minor rewriting to support multiple sextupole magnets, and the more realistic extraction method (extraction in several slices). The sextupole strength was increased again in steps through the strength factor (S_{fact}). The positions of the sextupole magnets and the ZS were fixed to their actual value in the SPS, and the adjustable parameters were the massless septum's longitudinal position s, its transverse position x and field gradient g.

8.3.1 Baseline ($\mathrm{S_{fact}} = 1$)

This case corresponds to the original extraction used in the SPS (without chromatic effects as described above). The extraction plot and the histogram of particle positions are visible in Fig. 8.7.

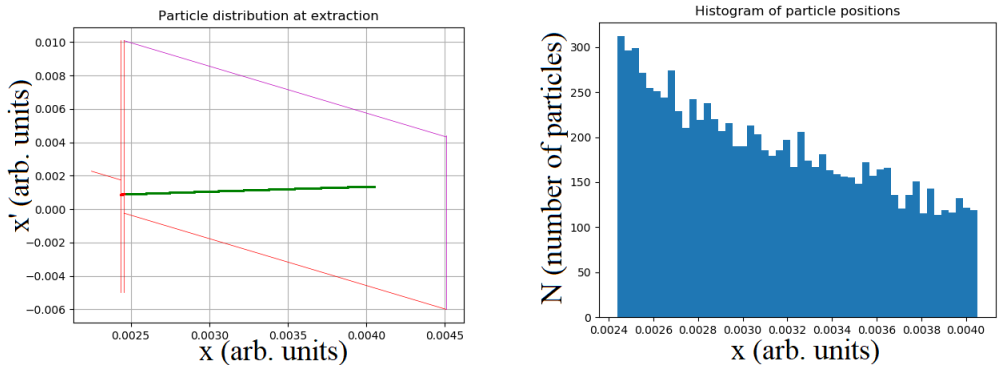

Figure 8.7: Extraction plot and histogram of the particles at $S_{fact} = 1$.

The number of lost and stable particles are 409 and 729, respectively. The baseline efficiency in this study is:

$$\eta = 0.9559$$

The number of stable particles is much higher than in the first study, but they are taken out of the statistics when calculating the efficiency.

8.3.2 Extraction at increased $\mathrm{S_{fact}}$

A few example extraction plots and corresponding histograms of particle positions are visible in Fig. 8.8-8.12. The results are discussed in the next section.

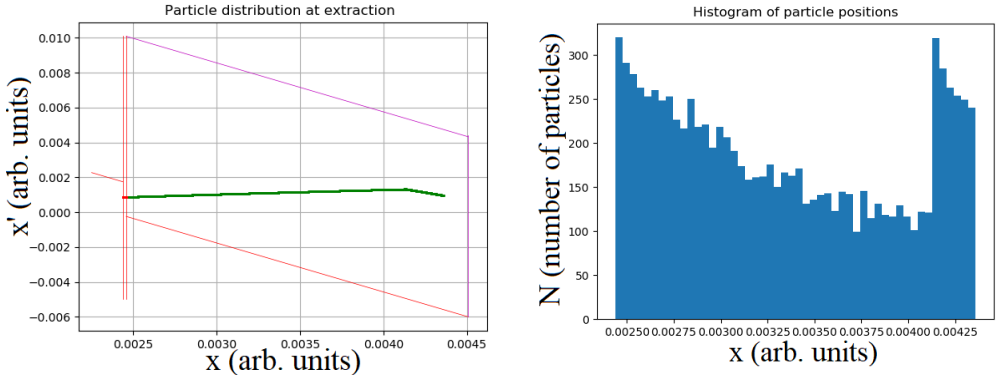

Figure 8.8: Extraction plot and histogram of the particles at $S_{fact} = 1.5$.

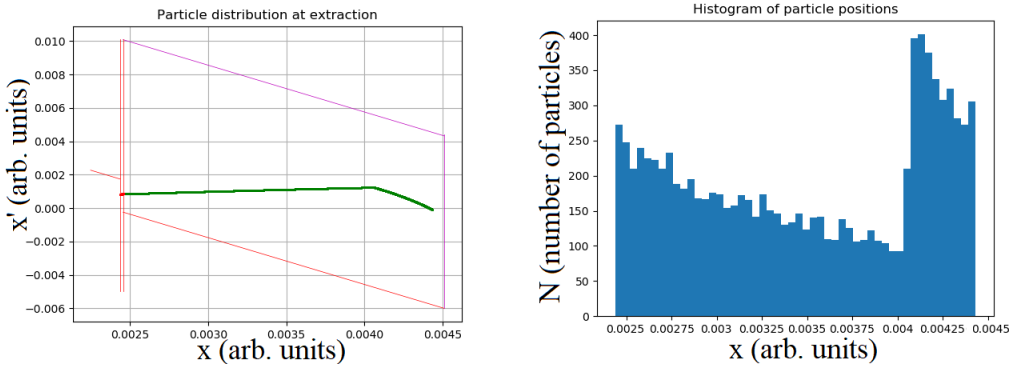

Figure 8.9: Extraction plot and histogram of the particles at $S_{fact} = 1.8$.

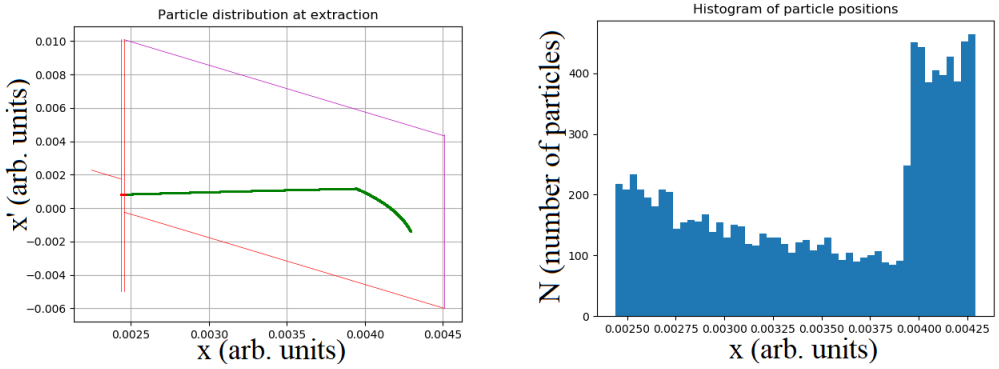

Figure 8.10: Extraction plot and histogram of the particles at $S_{fact} = 2.0$.

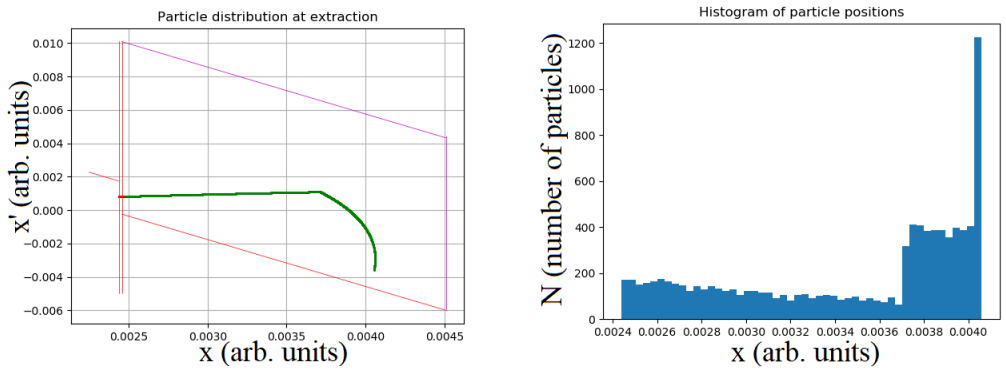

Figure 8.11: Extraction plot and histogram of the particles at $S_{fact} = 2.2$.

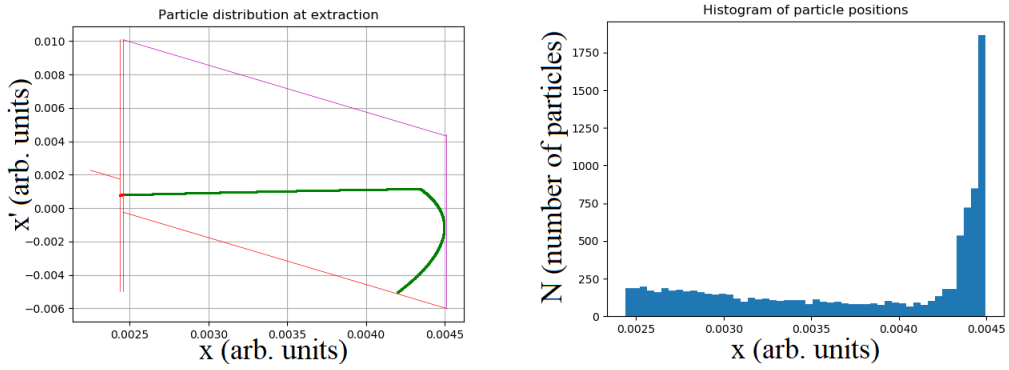

Figure 8.12: Extraction plot and histogram of the particles at $S_{fact} = 2.4$.

8.4 Conclusion of the second study

The results of the second study are summarized in Table 8.2. and Fig 8.13.

Table 8.2: Results of optimization in the second study.

Strength factor	Wires	Extracted	Remaining	Efficiency
1	409	8862	729	0.9559
1.1	368	8942	690	0.9605
1.2	358	9026	616	0.9619
1.3	348	9087	565	0.9631
1.4	321	9144	535	0.9661
1.5	308	9171	521	0.9675
1.6	272	9264	464	0.9715
1.7	277	9315	408	0.9711
1.8	264	9343	393	0.9725
1.9	234	9365	401	0.9756
2.0	228	9408	364	0.9763
2.1	213	9455	332	0.9780
2.2	212	9455	333	0.9781
2.3	214	9487	299	0.9780
2.4	186	9489	325	0.9808
2.5	510	9188	302	0.9474
2.6	967	8755	278	0.9005

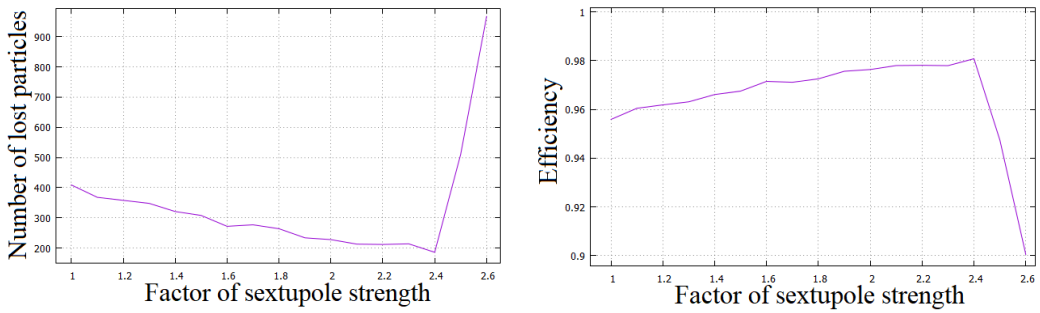

Figure 8.13: Number of lost particles (left) and the efficiency of the slow extraction (right) as a function of the strength factor in the second study.

The highest strength factor of $S_{fact} = 2.4$ is not feasible in reality due to the difficulty with extremely precise parameter tuning. The position and integrated gradient of the massless septum would need the ideally calculated value, with x tolerance less than $10\ \mu\mathrm{m}$.

The limitation is again the nonlinearity of the separatrix arm, although since in this study the arm bends downwards (reason for this is discussed above), the limit is much lower ($S_{fact} = 2.4$ instead of $S_{fact} = 4.5$).

The results of the simulation seem to be promising, already if the sextupole strength is increased by a factor of 2 the losses are reduced by a factor of 1.8. This results in a significant efficiency increase, and in combination with other loss reduction methods (e.g. diffuser, dynamic bump) it might be able to satisfy the needs of the fixed target experiments in the Northern Area.

Since the SPS optics will probably not be changed in order to increase slow extraction efficiency, this second study is important, since it gives a first estimate of the possible loss reduction using the concept of phase space folding by a massless septum.

9

Outlook

Increasing the spiral step (through increasing the sextupole strength) increases the beam size, and it is a question whether it fits into the ring aperture. This question was not studied in this work but probably needs to be the next step of the study. However, some suggestions have already come up for the case if the aperture limits the usable sextupole strength. Since the sextupole kick is distributed around the ring, the massless septum kick can also be distributed to more than one places, this way the beam size is not increased throughout the ring, but the particle density at the wires is still reduced. Further work is needed to study if a solution like this would work at all.

Another question is the effect of momentum spread and chromatic effects. Adding longitudinal momentum spread to the simulation would probably not affect feasibility, only change the achievable efficiency to some extent.

Due to the concept showing promising results a follow-up of the study is planned as part of a PhD topic at CERN.

10

Acknowledgement

This work would not be possible without the continuous support of my supervisor Daniel Barna, who involved me in his research and taught me a lot about accelerator physics, not even being afraid to spend his free time with me. He trusted me with important decisions, right from the beginning of us working together.

I also want to say thank you to the supervisor of my CERN Summer Student project Christoph Wiesner, who was helping me a lot even after I left CERN. Special thanks to Matthew Alexander Fraser, and Linda Susanne Stoel for the never ending patience towards me, and all the help they gave to help me succeed with the project. And last but not least I have to thank all the members of the TE-ABT-BTP section for making me feel comfortable joining a new environment.

Bibliography

[1] Accelerators for Society website, http://www.accelerators-for-society.org/

[2] MedAustron website, https://www.medaustron.at/en/particle-therapy

[3] Demortier G. (2005) Ion Beam Techniques for the Non-destructive Analysis of Archaelogical Materials. In: Uda M., Demortier G., Nakai I. (eds) X-rays for Archaeology. Springer, Dordrecht

[4] ISIS Neutron and Muon Source website, https://www.isis.stfc.ac.uk/Pages/How-does-the-antibiotic-amphotericin-work.aspx

[5] CERN Accelerator Complex, https://home.cern/about/accelerators

[6] NA61/SHINE page of CERN website, https://home.cern/about/experiments/na61shine

[7] Wikipedia page of particle accelerators, https://en.wikipedia.org/wiki/Particle_accelerator

[8] Concept of cyclotron, http://hyperphysics.phy-astr.gsu.edu/hbase/magnetic/cyclot.html

[9] W. Barletta, US Particle Accelerator School, 2011, Introduction to accelerator optics, http://uspas.fnal.gov/materials/11ODU/Into.pdf

[10] J. Holmes, S. Henderson, Y. Zhang, US Particle Accelerator School, 2009, Transverse Beam Optics, Part I, http://uspas.fnal.gov/materials/09VU/Lecture6.pdf

[11] B. Holzer, Introduction to Transverse Beam Optics II., https://cas.web.cern.ch/sites/cas.web.cern.ch/files/lectures/darmstadt-2009/holzer-2.pdf

[12] D. Barna, Prticle accelerators (HUN), https://wigner.mta.hu/~barna/content/Lectures/R%C3%A9szecskegyors%C3%ADt%C3%B3k%20-%20bevezet%C3%A9s.pdf

[13] V. Kain, Introduction to Accelerator Physics IV., CERN Summer School 2017, https://indico.cern.ch/event/632093/attachments/1487045/2309777/summer_students_vk2017_p4.pdf

[14] S. Guiducci, Chromaticity, Frascati National Laboratories - INFN, Frascati, Italy, https://cds.cern.ch/record/398300/files/p191.pdf

[15] B. Goddard, Injection and extraction, CERN Accelerator School, 2010, https://indico.cern.ch/event/173359/contributions/275955/attachments/218773/306407/Handouts-InjectionExtraction.pdf

[16] National research foundation website, http://tlabs.ac.za/?page_id=44

[17] M. A. Fraser, B. Goddard, SPS slow-extraction: Challenges and possibilities for improvement, https://indico.cern.ch/event/523655/contributions/2246434/attachments/1332085/2002352/MFraser_PBC_SE_v4.pdf

[18] B. Goddard et. al., Passive diffuser studies and design, https://indico.cern.ch/event/639766/contributions/2750896/attachments/1555304/2445586/Passive_diffuser_studies_and_design.pdf

[19] M. A. Fraser et. al., Experimental results of crystal-assisted slow extraction at the SPS, IPAC'17 proceeding, http://accelconf.web.cern.ch/AccelConf/ipac2017/papers/mopik048.pdf

[20] M. A. Fraser, L. S. Stoel, F. M. Velotti, SPS MD2128: Implementation of a dynamic extraction bump in LSS2, https://indico.cern.ch/event/678569/contributions/2779307/attachments/1553368/2442320/MFraser_DB_rMPP.pdf

[21] L. S. Stoel, et. al., Phase space folding studies for beam loss reduction during resonant slow extraction at the CERN SPS, IPAC'17 proceeding, http://inspirehep.net/record/1626373/files/mopik046.pdf

[22] Y. Yonemura, et. al., Beam extraction of the POP FFAG with a massless septum, IPAC'03 proceeding, http://accelconf.web.cern.ch/AccelConf/p03/PAPERS/TPPB028.PDF